MOX-Report No. 58/2022

Modeling isovolumetric phases in cardiac flows by an Augmented Resistive Immersed Implicit Surface Method

Zingaro, A.; Bucelli, M.; Fumagalli, I.; Dede', L; Quarteroni, A.

MOX, Dipartimento di Matematica
Politecnico di Milano, Via Bonardi 9 - 20133 Milano (Italy)

mox-dmat@polimi.it http://mox.polimi.it

Received: Added at production | Revised: Added at production | Accepted: Added at production

DOI: xxx/xxxx

ARTICLE TYPE

Modeling isovolumetric phases in cardiac flows by an Augmented Resistive Immersed Implicit Surface Method

Alberto Zingaro[‡1] | Michele Bucelli[‡*1] | Ivan Fumagalli[1] | Luca Dede'[1] | Alfio Quarteroni[1,2]

[1]MOX, Laboratory of Modeling and Scientitic Computing, Dipartimento di Matematica , Politecnico di Milano, Piazza Leonardo da Vinci, 32, 20133, Milano, Italy

[2]Institute of Mathematics, École Polytechnique Fédérale de Lausanne, Station 8, Av. Piccard, CH-1015 Lausanne, Switzerland (Professor Emeritus).

Correspondence
*Michele Bucelli, Email: michele.bucelli@polimi.it

[‡] Alberto Zingaro and Michele Bucelli equally contributed to this work.

Summary

A major challenge in the computational fluid dynamics modeling of the heart function is the simulation of isovolumetric phases when the hemodynamics problem is driven by a prescribed boundary displacement. During such phases, both atrioventricular and semilunar valves are closed: consequently, the ventricular pressure may not be uniquely defined, and spurious oscillations may arise in numerical simulations. In this paper, we propose a suitable modification of the Resistive Immersed Implicit Surface (RIIS) method (Fedele et al., 2017) by introducing a reaction term to correctly capture the pressure transients during isovolumetric phases. The method, that we call Augmented RIIS (ARIIS) method, extends the previously proposed ARIS method (This et al., 2020) to the case of a mesh which is not body-fitted to the valves. We test the proposed method on two different benchmark problems, including a new simplified problem that retains all the characteristics of a heart cycle. We apply the ARIIS method to a fluid dynamics simulation of a realistic left heart geometry, and we show that ARIIS allows to correctly simulate isovolumetric phases, differently from standard RIIS method.

KEYWORDS:
Cardiac Hemodynamics, Valves, Cardiac Modeling

1 | INTRODUCTION

During the heart cycle, there are two phases in which all cardiac valves are closed and the action of the ventricular displacement affects blood pressure without a net flow. In the left ventricle (the same applies for the right part of the heart), during the *isovolumetric contraction*, the intraventricular pressure raises up to the point in which the aortic valve open for the systolic ejection, while in the *isovolumetric relaxation* the ventricular pressure decreases until reaching the atrial one, thus leading to the opening of the mitral valve. Cardiac valve dynamics is mainly driven by transvalvular pressure drop[1]. Hence, an accurate modeling of the isovolumetric phases in which the intraventricular pressure undergoes rapid changes is an essential prerequisite to capture valve opening and closing, and to properly model their effect on the flow.

The behavior of blood pressure in the heart chambers is determined by the contraction and relaxation of the myocardium. With this in mind, Fluid-Structure Interaction (FSI) models coupling the blood flow with the heart mechanics have been proposed in the literature[2,3,4,5,6,7,8], or even more realistic electrophysiology-mechanics-hemodynamics models as in, e.g., [9,10,11,12]. However, these coupled models typically entail a high computational cost, and they require a challenging calibration of a huge number of physical parameters, especially in pathological conditions. Because of this, uncoupled (or one-way coupled) approaches

	conforming mesh	non-conforming mesh
no isovolumetric phases	RIS [32]	RIIS [56]
isovolumetric phases	ARIS [24]	ARIIS

TABLE 1 Features characterizing the RIS, RIIS, ARIS and ARIIS methods.

have been proposed, to address the sole Computational Fluid Dynamics (CFD) component of the system, with the ventricular displacement prescribed as data coming from analytical functions [13,14,15,16,17,18], clinical measurements [19,20,21,22], or from electromechanical simulations [23,24,25]. Such models mainly differ in the treatment of the valve geometry and dynamics. Mesh-conforming approaches are based on a classical Arbitrary Lagrangian-Eulerian formulation of the flow equations [26,27,28,29,30], and they include the Resistive Immersed Surface (RIS) method [31,32] and different XFEM/cutFEM methods [33,34,35,36,37,38,39]. All of these methods sharply track the valve surfaces, but they entail possible issues regarding large mesh deformations and topological changes at valve closure [40]. On the other hand, Eulerian approaches, such as the immersed boundary method [41,42,43,44,45,46,47,48], the fictitious domain method [49,50,51,52,53,54,55] or the Resistive Immersed Implicit Surface (RIIS) method [56,19], hinge upon an implicit representation of the leaflets and do not require mesh conformity between the fluid domain and the valves. For further details and comparisons among different valve models, we refer the reader to [57,58,59].

In most of the abovementioned simulations, however, the isovolumetric phases of the heartbeat are neglected due to the non-unique definition of pressure in the ventricle when all valves are closed [60,61,24,62,25]. This shortcoming is related to the absence of a stress condition on the fluid domain, that would otherwise ensure a correct description of the pressure during isovolumetric phases. This is observed for instance in [3,6,11,7,8], where fully coupled FSI models are used.

Some studies have circumvented this issue by introducing a slight compressibility of blood – see, e.g., [63,7]. However, this assumption may affect the simulation results also in the ejection and filling phases, and the assumption of blood incompressibility is quite established in the cardiovascular modeling community [62,64,65,66]. A way to overcome pressure non-determination, while preserving incompressibility, is provided by the Augmented Resistive Immersed Surface (ARIS) proposed in [24]: when both the mitral and the aortic valves are closed, the RIS method is augmented with a source term concentrated on the valves, to impose a prescribed value for the pressure.

In this work, we introduce an *Augmented Resistive Immersed Implicit Surface* (ARIIS) method that extends the ARIS capability of treating isovolumetric phases to the framework of the RIIS method, thus supporting a mesh that is not conforming with the valves (cf. Table 1). To quantitatively assess the results of the method, we propose a simulation setting in a simplified geometry that retains all the characteristics of the heart cycle and may be employed as a benchmark for cardiac hemodynamic solvers. Moreover, we discuss the application of our method to a realistic geometry of the left heart, with a prescribed displacement coming from electromechanical simulations.

The structure of the paper is the following. In Section 2, we recall the RIIS method and derive the ARIIS method to prescribe the intraventricular pressure. Then, in Section 3, we assess our new method in different scenarios: first, in Section 3.1, we analyze the idealized case discussed in [24]; then, in Section 3.2, we propose a simplified benchmark setting entailing ventricular contraction; finally, a cardiac case in a realistic geometry is considered in Section 3.3.

2 | MATHEMATICAL MODEL

In this section, we describe the cardiac hemodynamic model and we introduce a new augmented version of the RIIS method. Specifically, Section 2.1 is devoted to the Navier-Stokes equations in ALE framework with RIIS modeling of valves, and Section 2.2 to the derivation of the ARIIS method.

2.1 | The RIIS method for Navier-Stokes equations in ALE form

In heart chambers, blood can be considered as an incompressible, viscous and Newtonian fluid [67]. Let $\mathbf{u} : \Omega_t \times (0,T) \to \mathbb{R}^3$ and $p : \Omega_t \times (0,T) \to \mathbb{R}$ be the fluid velocity and pressure, respectively, where T is the final computational time, and Ω_t the domain in current configuration at time t, with $t \in (0,T)$. The domain at any time t is defined in terms of a displacement field $\mathbf{d} : \Omega_0 \times (0,T) \to \mathbb{R}^3$ as follows:

$$\Omega_t = \left\{ \mathbf{x} \in \mathbb{R}^3 : \mathbf{x} = \mathbf{x}_0 + \mathbf{d}(\mathbf{x}_0, t), \mathbf{x}_0 \in \Omega_0 \right\} .$$

Furthermore, we denote by $\mathbf{u}_{\text{ALE}} : \Omega_t \times (0,T) \to \mathbb{R}^3$ the ALE velocity[68,69] and we compute it by deriving $\mathbf{d}$ with respect to time. The domain displacement is the solution of the following harmonic extension problem:

$$\begin{cases} -\boldsymbol{\nabla} \cdot (K \boldsymbol{\nabla} \mathbf{d}) = \mathbf{0} & \text{in } \Omega_0 \times (0,T), \quad (1a) \\ \mathbf{d} = \mathbf{d}_{\partial\Omega}(\mathbf{x},t) & \text{on } \partial\Omega_0 \times (0,T), \quad (1b) \end{cases}$$

where $\mathbf{d}_{\partial\Omega} : \partial\Omega_0 \times (0,T) \to \mathbb{R}^3$ is the boundary displacement (which is prescribed), and K is a stiffness tensor field introduced to avoid distortion of mesh elements.

To model the cardiac valves with the RIIS method, we consider a surface Γ_{k} immersed in Ω_t, with $\text{k} \in \mathcal{I}_{\text{v}}$ (the set of immersed surfaces). We impose kinematic coupling between the surface and the fluid by penalizing the mismatch between the relative fluid velocity $\mathbf{u} - \mathbf{u}_{\text{ALE}}$ and the velocity of the immersed surface $\mathbf{u}_{\Gamma_{\text{k}}}$. Each surface is implicitly described by a signed distance function $\varphi_{\text{k}} : \Omega_t \times (0,T) \to \mathbb{R}$, such that $\Gamma_{\text{k}} = \left\{ \mathbf{x} \in \Omega_t \, : \, \varphi_{\text{k}}(\mathbf{x}) = 0 \right\}$, for all $\text{k} \in \mathcal{I}_{\text{v}}$. Γ_{k} is characterized by a resistance coefficient R_{k} and a parameter ε_{k} representing the half-thickness of the valve. The penalization is imposed in a narrow layer around Γ_{k}, represented by the following smoothed Dirac delta function:

$$\delta_{\text{k}}(\varphi_{\text{k}}(\mathbf{x})) = \begin{cases} \dfrac{1 + \cos\left(\pi \varphi_{\text{k}}(\mathbf{x}) / \varepsilon_{\text{k}}\right)}{2\varepsilon_{\text{k}}} & \text{if } |\varphi_{\text{k}}(\mathbf{x})| \le \varepsilon_{\text{k}}, \\ 0 & \text{if } |\varphi_{\text{k}}(\mathbf{x})| > \varepsilon_{\text{k}}, \end{cases}$$

with $\mathbf{x} \in \Omega_t$ and for all $\text{k} \in \mathcal{I}_{\text{v}}$. For additional details on the RIIS method, we refer the reader to[56,19].

The incompressible Navier-Stokes equations in the ALE framework with RIIS modeling of cardiac valves read as follows[19]:

$$\begin{cases} \rho \left(\dfrac{\partial \mathbf{u}}{\partial t} + \left(\left(\mathbf{u} - \mathbf{u}_{\text{ALE}} \right) \cdot \boldsymbol{\nabla} \right) \mathbf{u} \right) - \boldsymbol{\nabla} \cdot \left(\mu (\boldsymbol{\nabla} \mathbf{u} + \boldsymbol{\nabla}^T \mathbf{u}) \right) + \boldsymbol{\nabla} p + \displaystyle\sum_{\text{k} \in \mathcal{I}_{\text{v}}} \frac{R_{\text{k}}}{\varepsilon_{\text{k}}} \delta_{\text{k}}(\varphi_{\text{k}})(\mathbf{u} - \mathbf{u}_{\text{ALE}} - \mathbf{u}_{\Gamma_{\text{k}}}) = \mathbf{0} & \text{in } \Omega_t \times (0,T), \quad (2a) \\ \boldsymbol{\nabla} \cdot \mathbf{u} = 0 & \text{in } \Omega_t \times (0,T), \quad (2b) \end{cases}$$

endowed with suitable initial and boundary conditions. We denote the different terms appearing in (2a) as follows:

- inertial term: $\boldsymbol{\mathcal{I}}(\mathbf{u}) = \rho \left(\dfrac{\partial \mathbf{u}}{\partial t} + \left(\left(\mathbf{u} - \mathbf{u}_{\text{ALE}} \right) \cdot \boldsymbol{\nabla} \right) \mathbf{u} \right)$;
- viscous term: $\boldsymbol{\mathcal{D}}(\mathbf{u}) = \boldsymbol{\nabla} \cdot \left(\mu (\boldsymbol{\nabla} \mathbf{u} + \boldsymbol{\nabla}^T \mathbf{u}) \right)$;
- resistive term: $\boldsymbol{\mathcal{R}}(\mathbf{u}) = \displaystyle\sum_{\text{k} \in \mathcal{I}_{\text{v}}} \frac{R_{\text{k}}}{\varepsilon_{\text{k}}} \delta_{\text{k}}(\varphi_{\text{k}})(\mathbf{u} - \mathbf{u}_{\text{ALE}} - \mathbf{u}_{\Gamma_{\text{k}}})$.

2.2 | The ARIIS method

In this section, we derive the ARIIS method starting from the equations of the fluid model. To keep the notation light, we drop henceforth the explicit dependence on time of the domain and its subsets.

The left heart can be schematically outlined as a three-chambers domain as sketched in Figure 1: the Left Atrium (LA) Ω_{LA}, the Left Ventricle (LV) Ω_{LV} and the Ascending Aorta (AA) Ω_{AA}. These chambers are separated by two surfaces representing the Mitral Valve (MV) Γ_{MV} and the Aortic Valve (AV) Γ_{AV}, thus $\mathcal{I}_{\text{v}} = \{\text{MV}, \text{AV}\}$.

We denote by Ω the whole domain, such that $\overline{\Omega} = \overline{\Omega_{\text{LA}}} \cup \overline{\Omega_{\text{LV}}} \cup \overline{\Omega_{\text{AA}}}$. The domain boundary $\partial\Omega$ is partitioned into the inlet section Σ^{in}, the outlet section Σ^{out} and the wall Σ^{wall}, as shown in Figure 1. We introduce the sets

$$\Omega_{\text{k}} = \left\{ \mathbf{x} \in \Omega : \, \text{dist}(\mathbf{x}, \Gamma_{\text{k}}) = \min_{\mathbf{y} \in \Gamma_{\text{k}}} \|\mathbf{x} - \mathbf{y}\| < \varepsilon_{\text{k}} \}, \qquad \text{k} \in \{\text{MV}, \text{AV}\} \right\}, \quad (3)$$

where ε_{k} is the half thickness of Ω_{k} (characterizing the RIIS method and already introduced in Section 2.1), banded in Figure 1, for $\text{k} \in \{\text{MV}, \text{AV}\}$. These regions have nontrivial intersections with the chambers defined above.

With reference to Figure 2, we introduce two geometric assumptions that will be used in the derivation of the augmented method of Section 2.2.

Assumption 1. (Flat valve surfaces) For $\text{k} \in \{\text{MV}, \text{AV}\}$, the normal vector $\mathbf{n}_{\text{k}}$ to the valve surface Γ_{k} (pointing outwards w.r.t. Ω_{LV}) is constant over Γ_{k}.

Remark 1. If Assumption 1 is satisfied, we can define a constant vector field extending the definition of the valve normal vector $\mathbf{n}_{\text{k}}$ to the whole valve region Ω_{k} . We denote such field with the same symbol $\mathbf{n}_{\text{k}} : \Omega_{\text{k}} \to \mathbb{R}^3, \text{k} \in \{\text{MV}, \text{AV}\}$.

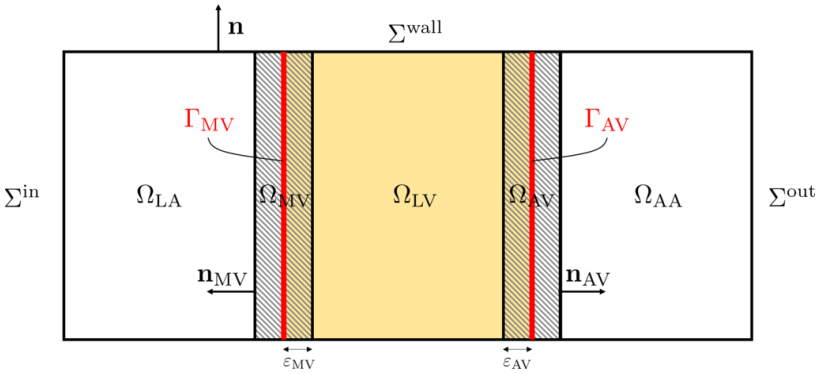

FIGURE 1 Sketch of the three-chambers domain Ω with its subsets and boundaries. In yellow Ω_{LV}, in white $\Omega_{\text{LA}}, \Omega_{\text{AA}}$, in striped pattern (partially overlapping $\Omega_{\text{LV}}, \Omega_{\text{LA}}, \Omega_{\text{AA}}$) the valve regions $\Omega_{\text{MV}}, \Omega_{\text{AV}}$. The latter are defined by the immersed surfaces Γ_{MV} and Γ_{AV} (in red) and the half-thicknesses ε_{k}, with $\text{k} \in \{\text{MV}, \text{AV}\}$.

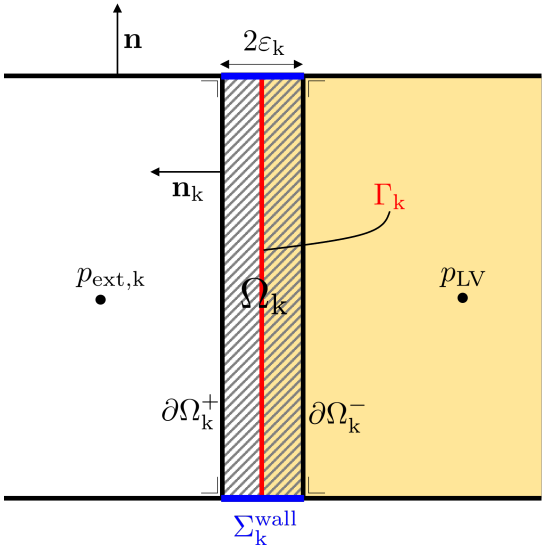

FIGURE 2 Sketch of the immersed surface Γ_{k} (red) with the corresponding valve region Ω_{k} (striped pattern) and its boundaries.

Assumption 2. (Valves orthogonal to the wall) By denoting with $\mathbf{n}$ the normal vector of $\partial\Omega$, $\mathbf{n}_{\text{k}} \cdot \mathbf{n} = 0$ on $\Sigma_{\text{k}}^{\text{wall}}$, for $\text{k} \in \{\text{MV}, \text{AV}\}$, where $\Sigma_{\text{k}}^{\text{wall}} = \Sigma^{\text{wall}} \cap \partial\Omega_{\text{k}}$.

Remark 2. By introducing $\partial\Omega_{\text{k}}^{-} = \partial\Omega_{\text{k}} \cap \Omega_{\text{LV}}$ and $\partial\Omega_{\text{k}}^{+} = \partial\Omega_{\text{k}} \setminus (\partial\Omega_{\text{k}}^{-} \cup \Sigma_{\text{k}}^{\text{wall}})$ (cfr. Figure 2) we observe that $|\partial\Omega_{\text{k}}^{-}| = |\partial\Omega_{\text{k}}^{+}| = |\Gamma_{\text{k}}|$, $\text{k} \in \{\text{MV}, \text{AV}\}$.

Moreover, we make the following assumptions:

Assumption 3 (Constant pressure in the compartments)**.** Pressure is constant in space within $\Omega_{\text{LA}}, \Omega_{\text{LV}}$ and Ω_{AA}. We will denote the respective constant values with $p_{\text{LA}}(t)$, $p_{\text{LV}}(t)$ and $p_{\text{AA}}(t)$.

Assumption 4 (Negligible inertia and viscosity within valves)**.** For $\text{k} \in \{\text{MV}, \text{AV}\}$, inertial and viscous terms in (2a) are negligible in Ω_{k}: $\boldsymbol{\mathcal{I}}(\mathbf{u}) \approx \mathbf{0}$ and $\boldsymbol{\mathcal{D}}(\mathbf{u}) \approx \mathbf{0}$.

When MV and AV are closed, the intraventricular pressure is prone to spurious oscillations, due to the ventricle being fully enclosed by boundaries on which a Dirichlet-type condition on the velocity is imposed (either strongly or through the RIIS

penalty term). Thus, we augment Equation (2a) with a reaction term to impose $p^* : (0,T) \to \mathbb{R}$, a prescribed value of the ventricular pressure (constant in space by Assumption 3), that can be obtained, for instance, from an electromechanical simulation or from patient-specific measured data.

We assume the perturbation term to be in the form:

$$\sum_{k\in\{MV,AV\}} C_k \delta_k \mathbf{n}_k, \tag{4}$$

with $C_k \in \mathbb{R}$, for $k \in \{MV, AV\}$. This choice of the reaction term (4) is such that the augmented formulation acts on the valves only and does not perturb the momentum equation outside Ω_k.

The pertubation term represents the force that the blood exerts on the closed valves during isovolumetric phases. We derive it to enforce that the ventricular pressure matches the reference one p^*. Thus, following [24], we derive an estimation of the ventricular pressure $p_{LV}(t)$ when both valves are closed. The estimate will be used to determine the corrective term C_k in (4).

From (2a) and Assumption 4, we deduce

$$\boldsymbol{\nabla} p + \boldsymbol{\mathcal{R}}(\mathbf{u}) = \mathbf{0} \qquad \text{in } \Omega_k,$$

for all $k \in \{MV, AV\}$. Multiplying by $\mathbf{n}_k$ and integrating over Ω_k, we get

$$\int_{\Omega_k} (\boldsymbol{\nabla} p + \boldsymbol{\mathcal{R}}(\mathbf{u})) \cdot \mathbf{n}_k = 0.$$

By Assumption 1, we can take $\mathbf{n}_k$ out of the integral and integrate by parts the pressure term yielding

$$\left(\int_{\partial\Omega_k} p\mathbf{n} + \int_{\Omega_k} \boldsymbol{\mathcal{R}}(\mathbf{u}) \right) \cdot \mathbf{n}_k = 0,$$

$$\int_{\partial\Omega_k} p\mathbf{n} \cdot \mathbf{n}_k + \int_{\Omega_k} \boldsymbol{\mathcal{R}}(\mathbf{u}) \cdot \mathbf{n}_k = 0.$$

Using Assumptions 1 and 2, we get

$$\left(p_{LV} - p_{ext,k}\right) |\Gamma_k| - \int_{\Omega_k} \boldsymbol{\mathcal{R}}(\mathbf{u}) \cdot \mathbf{n}_k = 0, \tag{5}$$

where $p_{ext,k} = p_{LA}$ for $k = MV$ and $p_{ext,k} = p_{AA}$ for $k = AV$. Finally, summing (5) for both valves, we obtain:

$$\left(p_{LV} - p_{LA}\right) |\Gamma_{MV}| + \left(p_{LV} - p_{AA}\right) |\Gamma_{AV}| - \sum_{k\in\{MV,AV\}} \int_{\Omega_k} \boldsymbol{\mathcal{R}}(\mathbf{u}) \cdot \mathbf{n}_k = 0, \tag{6}$$

from which we derive

$$p_{LV} = \frac{1}{|\Gamma_{MV}| + |\Gamma_{AV}|} \left(|\Gamma_{MV}| p_{LA} + |\Gamma_{AV}| p_{AA} + \sum_{k\in\{MV,AV\}} \int_{\Omega_k} \boldsymbol{\mathcal{R}}(\mathbf{u}) \cdot \mathbf{n}_k \right). \tag{7}$$

Repeating these calculations including the perturbation term (4), (6) rewrites as

$$\sum_{k\in\{MV,AV\}} \left(\left(p_{LV} - p_{ext,k}\right) |\Gamma_k| - \int_{\Omega_k} \boldsymbol{\mathcal{R}}(\mathbf{u}) \cdot \mathbf{n}_k - C_k \int_{\Omega_k} \delta_k \right) = 0 \,,$$

so that, if the perturbation satisfies

$$\sum_{k\in\{MV,AV\}} \int_{\Omega_k} C_k \delta_k = \sum_{k\in\{MV,AV\}} \left((p^* - p_{ext,k}) |\Gamma_k| - \int_{\Omega_k} \boldsymbol{\mathcal{R}}(\mathbf{u}) \cdot \mathbf{n}_k \right), \tag{8}$$

then our estimate for p_{LV} becomes $p_{LV} = p^*$.

Observing that $\int_{\Omega_k} \delta_k = |\Gamma_k|$, a possible definition of the corrective term satisfying (8) is:

$$C_k(\mathbf{u}, p) = p^* - p_{ext,k} - \frac{1}{|\Gamma_{MV}| + |\Gamma_{AV}|} \sum_{k\in\{MV,AV\}} \int_{\Omega_k} \boldsymbol{\mathcal{R}}(\mathbf{u}) \cdot \mathbf{n}_k \,. \tag{9}$$

Thus, the ARIIS method consists in solving the following problem:

$$\begin{cases} \rho\left(\dfrac{\partial \mathbf{u}}{\partial t} + \left(\left(\mathbf{u}-\mathbf{u}_{\mathrm{ALE}}\right)\cdot\boldsymbol{\nabla}\right)\mathbf{u}\right) - \boldsymbol{\nabla}\cdot\left(\mu(\boldsymbol{\nabla}\mathbf{u}+\boldsymbol{\nabla}^T\mathbf{u})\right) + \boldsymbol{\nabla} p \\ \quad + \displaystyle\sum_{\mathrm{k}\in\{\mathrm{MV,AV}\}} \left(\frac{R_{\mathrm{k}}}{\varepsilon_{\mathrm{k}}}\delta_{\mathrm{k}}(\varphi_{\mathrm{k}})(\mathbf{u}-\mathbf{u}_{\mathrm{ALE}}-\mathbf{u}_{\Gamma_{\mathrm{k}}}) + \chi_{\mathrm{iso}}(t)C_{\mathrm{k}}(\mathbf{u},p)\delta_{\mathrm{k}}\mathbf{n}_{\mathrm{k}}\right) = \mathbf{0} & \text{in } \Omega_t\times(0,T), \quad (10a) \\ \boldsymbol{\nabla}\cdot\mathbf{u} = 0 & \text{in } \Omega_t\times(0,T), \quad (10b) \end{cases}$$

endowed with suitable initial and boundary conditions. $\chi_{\mathrm{iso}}(t)$ is a characteristic function equal to 1 during the isovolumetric phases, 0 otherwise: we activate the ARIIS correction term only when both valves are simultaneously closed. $\chi_{\mathrm{iso}}(t)$ can be prescribed a priori or be determined by pressure jump conditions (to determine the opening and closing of valves)[24].

3 | NUMERICAL RESULTS

In this section, we present and discuss the results on the ARIIS method by carrying out numerical simulations of three different problems. All three tests feature valves that open and close. In Section 3.1, we check the validity of our method by considering the simple problem introduced in[24] (Test A). In Section 3.2, we propose a new benchmark problem consisting of the flow in a compliant pipe with ventricle-like shortening (Test B). Finally, in Section 3.3, we apply our method to a cardiac case, i.e. the flow in a realistic left heart geometry (Test C).

The physical parameters for blood are density $\rho = 1.06\times10^3\,\mathrm{kg/m^3}$ and dynamic viscosity $\mu = 3.5\times10^{-3}\,\mathrm{kg/(m\cdot s)}$. In all the numerical experiments considered, we apply a null velocity initial condition. Furthermore, similarly to[19,25], we use a quasi-static approach by choosing $\mathbf{u}_{\Gamma_{\mathrm{k}}} = \mathbf{0}$.

We discretize (10) in space with piecewise linear Finite Elements (FE) for velocity and pressure ($\mathbb{P}_1-\mathbb{P}_1$) and in time with the backward Euler method. We employ a semi-implicit treatment of the non-linear term. In Section 3.1 and Section 3.2, we use a SUPG-PSPG stabilization[70]. Differently, in Section 3.3, we use the VMS-LES method acting as both a stabilization method and a turbulence model to account for the transition-to-turbulence flow regime typically occurring in cardiac flows[71,72,14]. The lifting problem (1) is discretized with linear FEs.

We carry out our numerical simulations in `lifex`[73†], a high-performance `C++` FE library developed within the iHEART project[‡], mainly focused on cardiac simulations and based on the `deal.II` finite element core[74,75,76].

3.1 | Test A: a simple benchmark problem

In this section, following[24], we consider a benchmark problem that was originally introduced to test the ARIS method in a simplified setting.

The domain is a cylinder of radius $R_{\mathrm{c}} = 0.01\,\mathrm{m}$ and length $L_{\mathrm{c}} = 0.1\,\mathrm{m}$. It is divided into three cylindrical compartments, representing, in an idealized context, the LA, LV and AA, of lengths $L_{\mathrm{LA}} = 0.02\,\mathrm{m}$, $L_{\mathrm{LV}} = 0.06\,\mathrm{m}$ and $L_{\mathrm{AA}} = 0.02\,\mathrm{m}$, respectively. Two planar surfaces represent the MV and AV. We solve in the time interval $[0,T]$, with $T = 0.2\,\mathrm{s}$.

The domain is discretized with a tetrahedral mesh of 75 933 elements, for a total of 56 684 degrees of freedom. The mesh is finer near to the immersed surfaces, to better capture their presence, with a minimum element diameter $h_{\min} = 1\,\mathrm{mm}$ and a maximum diameter $h_{\max} = 4.6\,\mathrm{mm}$ (see Fig. 3). Simulations ran in parallel using 4 cores of a local workstation, each with an Intel Core i5-9600K@3.70GHz processor.

Following[24], we impose a homogeneous and constant pressure of $p_{\mathrm{in}} = 0\,\mathrm{mmHg}$ at the inlet section, and a homogeneous and constant pressure of $p_{\mathrm{out}} = 75\,\mathrm{mmHg}$ at the outlet section. The displacement $\mathbf{d}_{\partial\Omega}$ of the lateral boundary is prescribed analytically

[†] https://lifex.gitlab.io/

[‡] iHEART - An Integrated Heart model for the simulation of the cardiac function, European Research Council (ERC) grant agreement No 740132, P.I. Prof. A. Quarteroni, 2017-2022

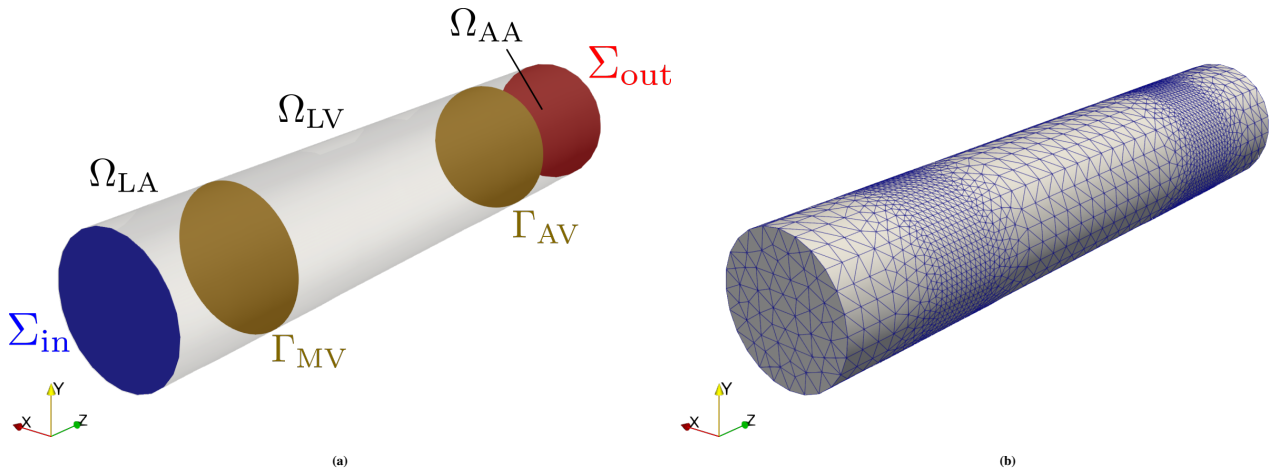

FIGURE 3 Test A. Domain for the cylinder test cases, with highlighted immersed and boundary surfaces (a); tetrahedral mesh for the cylinder test cases.

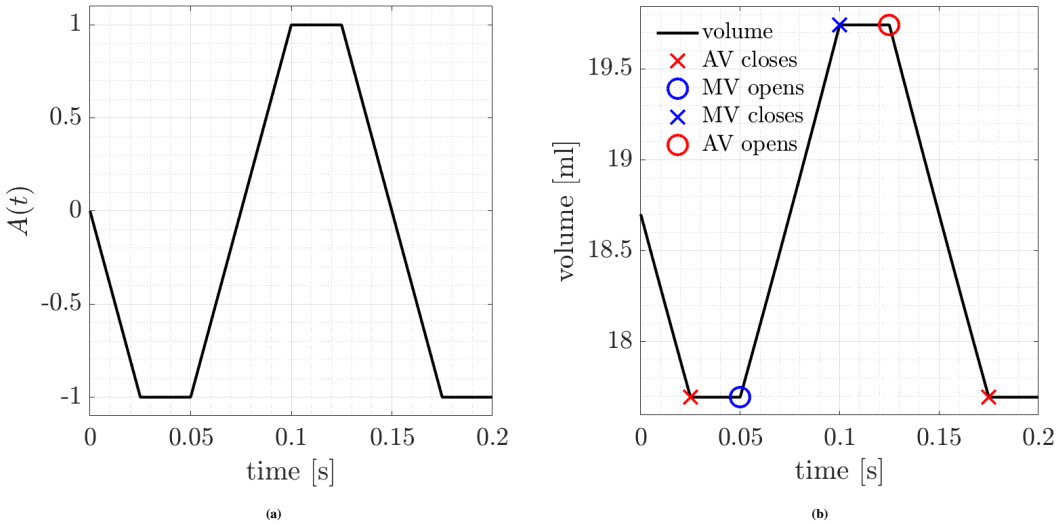

FIGURE 4 Test A. (a) Plot of the function $A(t)$ that defines the time evolution of the boundary displacement in the cylindrical toy problem. (b) The corresponding volume of the ventricular compartment with valve opening and closing times.

and mimics the contraction-relaxation cycle of a human ventricle. For a given point $\mathbf{x} = (x_1, x_2, x_3)^T$ and time t, it is defined as

$$\mathbf{d}_{\partial\Omega}(\mathbf{x}, t) = \begin{cases} \overline{w}\, A(t)\, \mathbf{e}_r(\mathbf{x}) \exp\left(-\dfrac{\left| x_3 - \frac{L_c}{2} \right|^2}{2\sigma^2} \right) & \text{if } x_3 \in [L_{LA}, L_{LA} + L_{LV}) \,, \\ \mathbf{0} & \text{otherwise,} \end{cases}$$

with

$$\mathbf{e}_r(\mathbf{x}) = \frac{(x_1, x_2, 0)^T}{\sqrt{x_1^2 + x_2^2}} \,.$$

$A(t)$ is the piecewise linear function depicted in Figure 4a. We set $\sigma = 0.015$ m and $\overline{w} = 4.6 \times 10^{-4}$ m, to have the same time evolution of volume as in[24] (see Fig. 4b). We take $K = I$ in (1).

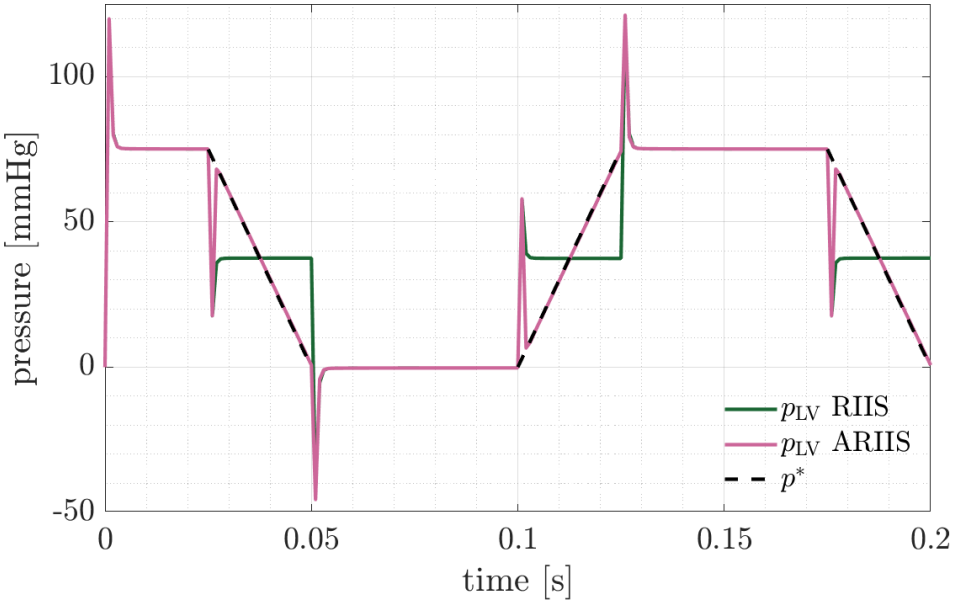

FIGURE 5 Test A. Ventricular and reference pressures for the cylindrical toy problem, with RIIS and ARIIS methods, using resistance $R = 10^4\,\mathrm{kg}/(\mathrm{m}\cdot\mathrm{s})$ and $\varepsilon = 0.002\,\mathrm{m}$.

We simulate the opening of a valve by instantaneously removing the corresponding surface from the domain. Valves are opened and closed at prescribed times, following the evolution of the volume of the ventricular compartment. The MV is closed when the simulation starts, while the AV is open. Closing and opening times are reported in Figure 4b.

In this setting, we carry out a comparison of the results obtained with the RIIS method against those obtained with the ARIIS method, using as reference pressure $p^*(t)$ a piecewise linear function. The evolution of ventricular pressure for both cases, computed with resistance $R = 10^4\,\mathrm{kg}/(\mathrm{m}\cdot\mathrm{s})$ and $\varepsilon = 0.002\,\mathrm{m}$, is reported in Figure 5. The plots show how the ARIIS method allows the ventricular pressure to accurately follow the provided reference pressure. The observed peaks are associated to the simplified and instantaneous way in which valves are opened and closed and to the explicit computation of the corrective term (4).

Moreover, we carry out a sensitivity analysis by varying the resistance coefficient R in the ARIIS method, to understand how the quality of the results is influenced by it. Results are reported in Figure 6. Although the resistance coefficient varies by several orders of magnitude, no difference is observed on the accuracy of the ventricular pressure. This is evident in particular in Figure 6b, reporting the relative pressure error

$$\frac{\max_{t\in T_{\mathrm{iso}}} |p_{\mathrm{LV}} - p^*|}{\max_{t\in T_{\mathrm{iso}}} |p^*|}\,, \tag{11}$$

where $T_{\mathrm{iso}} = \{t \in (0,T) \,:\, \chi_{\mathrm{iso}}(t) = 1\}$ is the set of times at which both valves are closed. The error is approximately equal to 8×10^{-3} regardless of the value of R. The ARIIS method, therefore, yields reliable pressure results also with high values of R, that ensure negligible spurious flow through the resistive surfaces.

Overall, the obtained results indicate that the ARIIS method is successful in its aim of producing a ventricular pressure that closely follows the prescribed reference evolution.

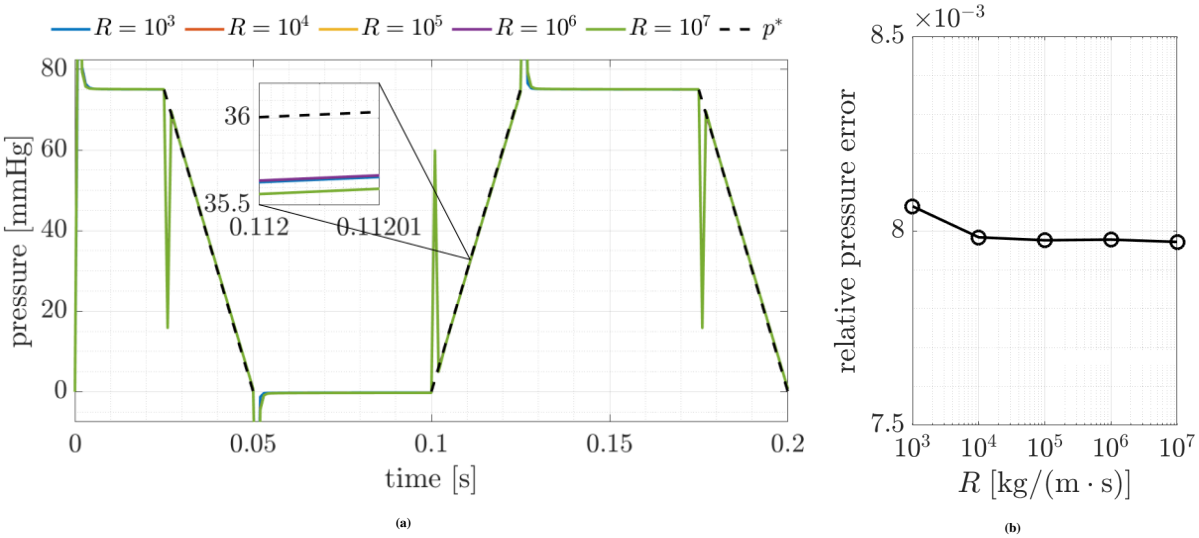

FIGURE 6 Test A. (a) Evolution of pressure with the ARIIS method with varying values of the resistance. (b) Relative error between the computed pressure during isovolumic phases and the reference pressure p^*.

3.2 | Test B: a benchmark problem including ventricular shortening

As an intermediate step towards cardiac simulations, we introduce a novel test case in a cylindrical domain that mimics the ventricular shortening during contraction. We use the same domain as in Section 3.1, but change the boundary displacement as follows:

$$\mathbf{d}_{\partial\Omega}(\mathbf{x},t) = \begin{cases} \mathbf{0} & \text{if } x_3 \in [0, L_{\mathrm{LA}}) \,, \\ \mathbf{d}^r_{\partial\Omega}(\mathbf{x},t) + \mathbf{d}^z_{\partial\Omega}(\mathbf{x},t) & \text{if } x_3 \in [L_{\mathrm{LA}}, L_{\mathrm{LA}} + L_{\mathrm{LV}}) \,, \\ (0,\ 0,\ L^*_{\mathrm{LV}}(t) - L_{\mathrm{LV}})^T & \text{if } x_3 \in [L_{\mathrm{LA}} + L_{\mathrm{LV}}, L) \,, \end{cases} \tag{12}$$

(13)

with

$$\mathbf{d}^r_{\partial\Omega}(\mathbf{x},t) = \left(R_{\mathrm{c}} + c(t) \sin\left(\frac{\pi(x_3 - L_{\mathrm{LA}})}{L_{\mathrm{LV}}} \right) \right) \mathbf{r}(\mathbf{x}) - \mathbf{x} \,, \tag{14}$$

$$\mathbf{d}^z_{\partial\Omega}(\mathbf{x},t) = \frac{x_3 - L_{\mathrm{LA}}}{L_{\mathrm{LV}}} (L^*_{\mathrm{LV}}(t) - L_{\mathrm{LV}}) \tag{15}$$

and

$$c(t) = \frac{4R_{\mathrm{c}}}{\pi} + \frac{\sqrt{16\, R_{\mathrm{c}}^2\, L^*_{\mathrm{LV}}(t)^2 - 2\,\pi\, L^*_{\mathrm{LV}}(t)\, \left(\pi\, L^*_{\mathrm{LV}}(t)\, R_{\mathrm{c}}^2 - V^*_{\mathrm{LV}}(t) \right)}}{\pi\, L^*_{\mathrm{LV}}(t)} \,. \tag{16}$$

In the above, $L^*_{\mathrm{LV}}(t)$ and $V^*_{\mathrm{LV}}(t)$ are prescribed time dependent functions for the ventricular length and volume, respectively. The displacement is such that, at any time t, the ventricular length and volume in the deformed configuration match the prescribed ones. We take $K = I$ in (1). Valve positions change over time following the domain displacement. Their opening and closing times are reported in Figure 7. The MV starts open, and the AV starts closed. Moreover, we set inlet and outlet boundary conditions to $p_{\mathrm{in}} = 0$ mmHg and $p_{\mathrm{out}} = 80$ mmHg, to replicate the typical range that characterizes the heart function.

Numerical simulations are run in parallel on the GALILEO100 supercomputer[§] at the CINECA supercomputing center, using 48 cores.

Figures 8 and 9 report snapshots of pressure and velocity in the solution, computed using RIIS and ARIIS. We can observe that the two methods yield equivalent results outside the isovolumetric phases. Differently, when both valves are closed, a

[§]528 computing nodes each 2 x CPU Intel CascadeLake 8260, with 24 cores each, 2.4 GHz, 384GB RAM. See https://wiki.u-gov.it/confluence/display/SCAIUS/UG3.3%3A+GALILEO100+UserGuide for technical specifications.

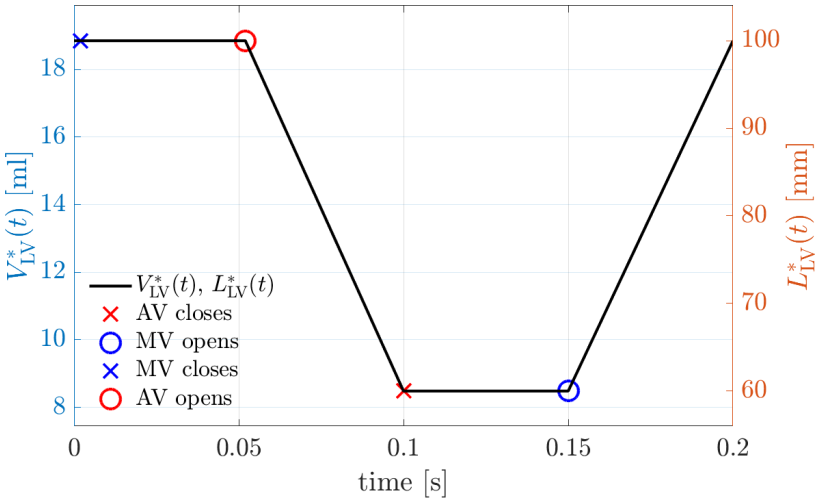

FIGURE 7 Test B. Prescribed ventricular volume $V^*_{LV}(t)$ (left axis) and length $L^*_{LV}(t)$ (right axis).

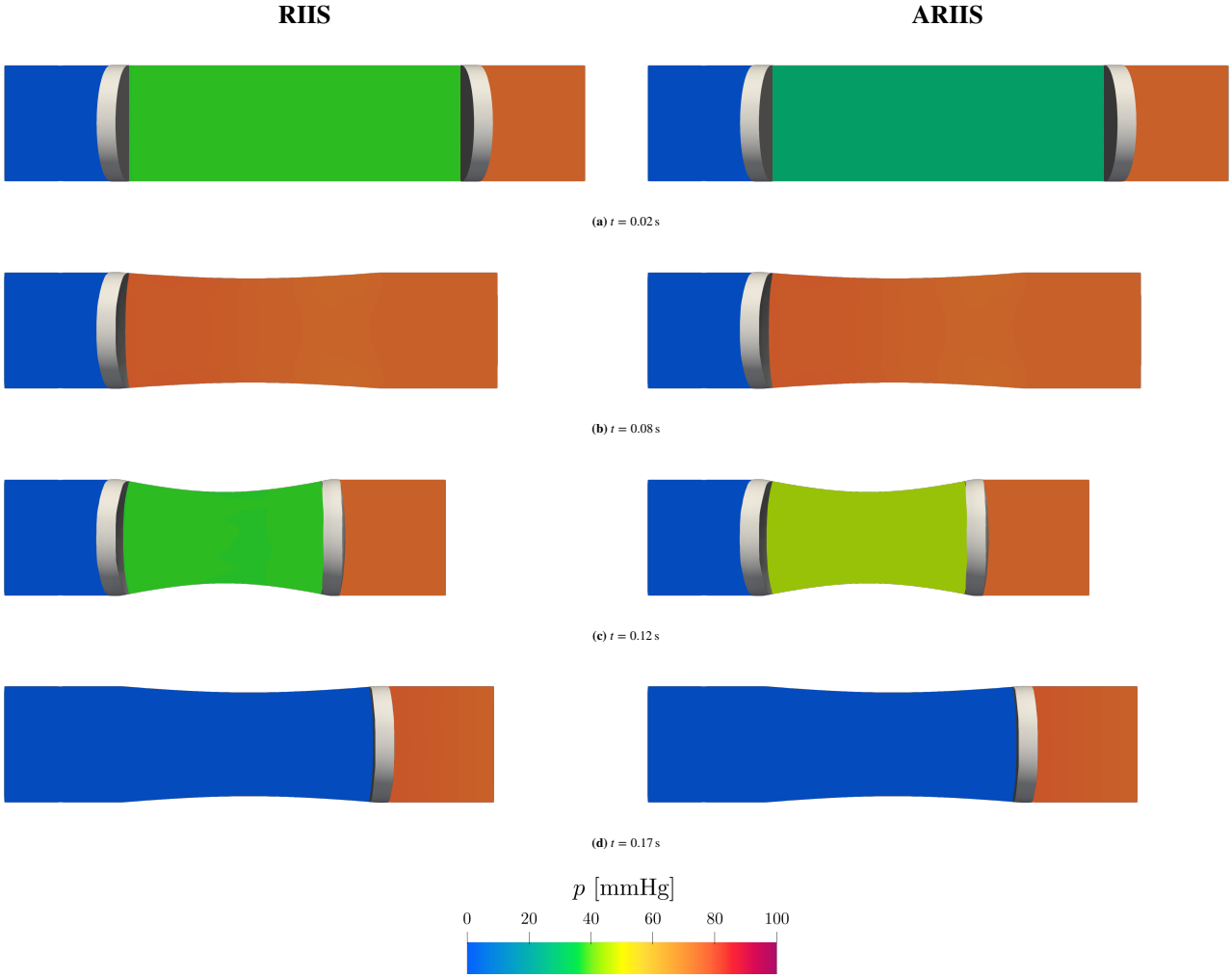

FIGURE 8 Test B. Snapshots of the pressure over one longitudinal slice of the domain, simulated using the RIIS (left) and ARIIS (right) method. The snapshots are taken at the midpoint of isovolumetric contraction (a), ejection (b), isovolumetric relaxation (c) and filling (d). The domain is warped according to the displacement **d** defined in (12).

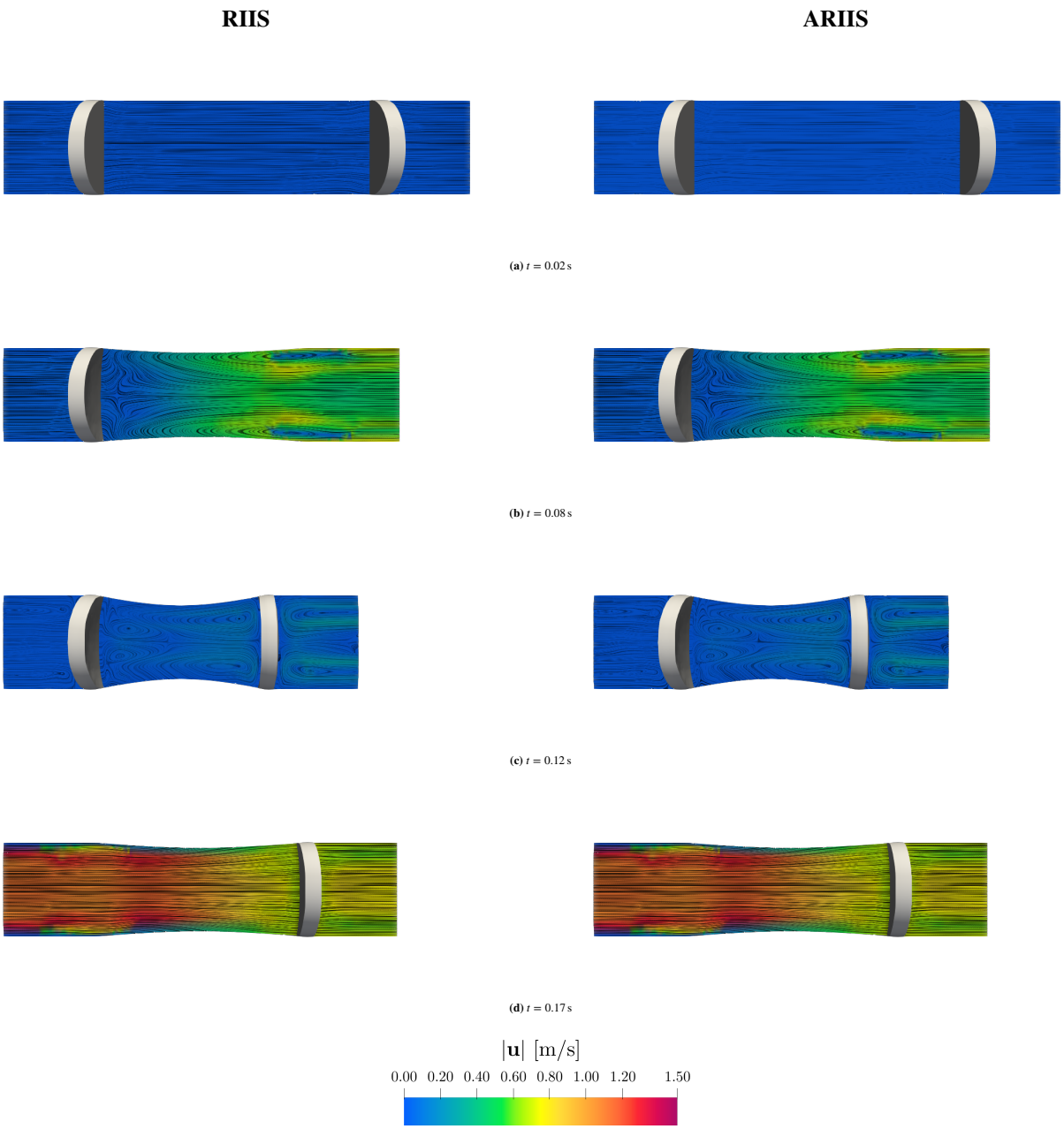

FIGURE 9 Test B. Snapshots of the velocity magnitude over one longitudinal slice of the domain, simulated using the RIIS (left) and ARIIS (right) methods. The snapshots are taken at the midpoint of isovolumetric contraction (a), ejection (b), isovolumetric relaxation (c) and filling (d). The domain is warped by the displacement **d** defined in (12), and the velocity magnitude is superimposed with the surface LIC rendering of the flow field.

considerably different pressure can be observed. Similar conclusions can be drawn from the plots reported in Fig. 10, representing the average ventricular pressure over time for Test B, using RIIS and ARIIS, setting $R = 10^4\,\mathrm{kg/(m \cdot s)}$ and $\varepsilon = 0.002\,\mathrm{m}$. The ARIIS simulation yields a pressure that closely follows the provided reference pressure p^* during isovolumetric phases. Conversely, outside the isovolumetric phases, the two methods correctly produce the same result.

We carry out numerical simulations with the ARIIS method by varying the resistance coefficient R over several orders of magnitude and computing the relative pressure error (11) during isovolumetric phases. We report the results in Fig. 11. As before, we observe that the reference pressure is matched accurately during isovolumetric phases, regardless of the value of R.

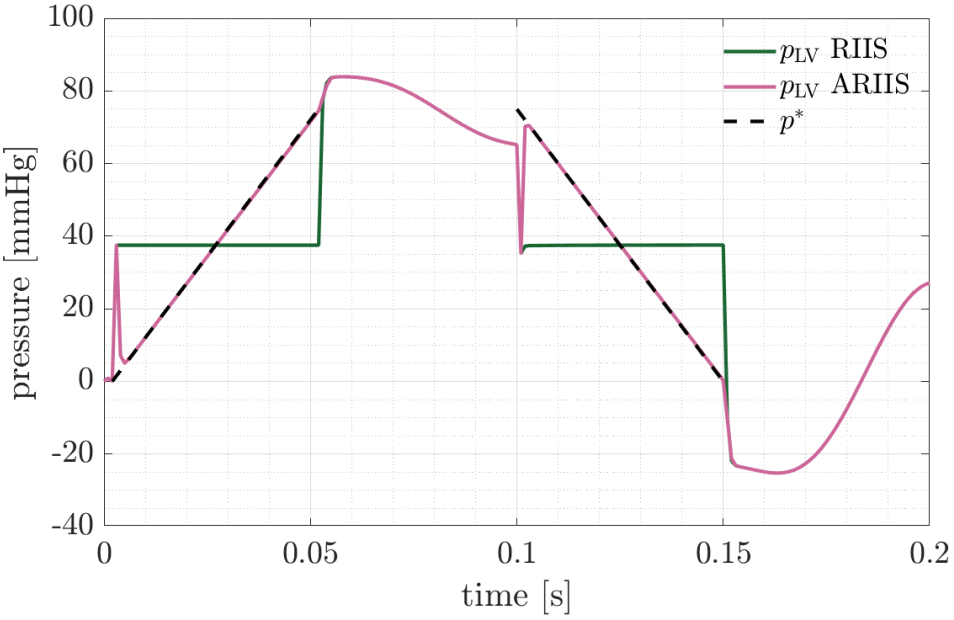

FIGURE 10 Test B. Ventricular and reference pressures, with RIIS and ARIIS methods, using resistance $R = 10^4\,\mathrm{kg/(m \cdot s)}$ and $\varepsilon = 0.002\,\mathrm{m}$.

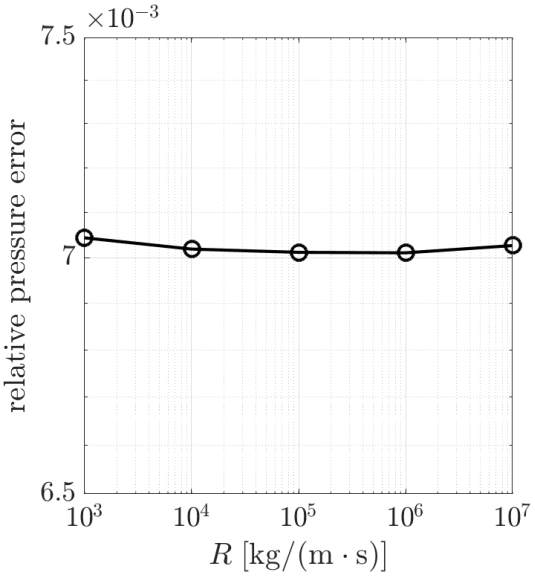

FIGURE 11 Relative error between the computed pressure during isovolumetric phases and the reference pressure p^*, with varying resistance R, $\varepsilon = 0.002\,\mathrm{m}$ and minimum mesh size $h_{\min} = 0.001\,\mathrm{m}$.

3.3 | Test C: application to a cardiac case

In this section, we apply the ARIIS method to a realistic cardiac case. We use the CFD model of a healthy left heart developed in[25]. It consists of the 3D fluid dynamics model (10) coupled to the surrounding circulation (described by a 0D closed-loop model[77,78,79]) and driven by a cardiac electromechanical model[79].

We consider a realistic left heart geometry provided by Zygote[80], representing an accurate 3D model of the heart obtained with CT scan data. We report the domain in Figure 12a: its boundary is split as $\partial\Omega_t = \Sigma^{\text{in}} \cup \Sigma^{\text{out}} \cup \Sigma_t^{\text{wall}}$, where Σ^{in} is the set of pulmonary veins inlet sections, Σ^{out} the outlet section of the ascending aorta and Σ_t^{w} the wall (endocardium). In addition, we display the immersed surfaces Γ_{MV} and Γ_{AV} in their closed configurations.

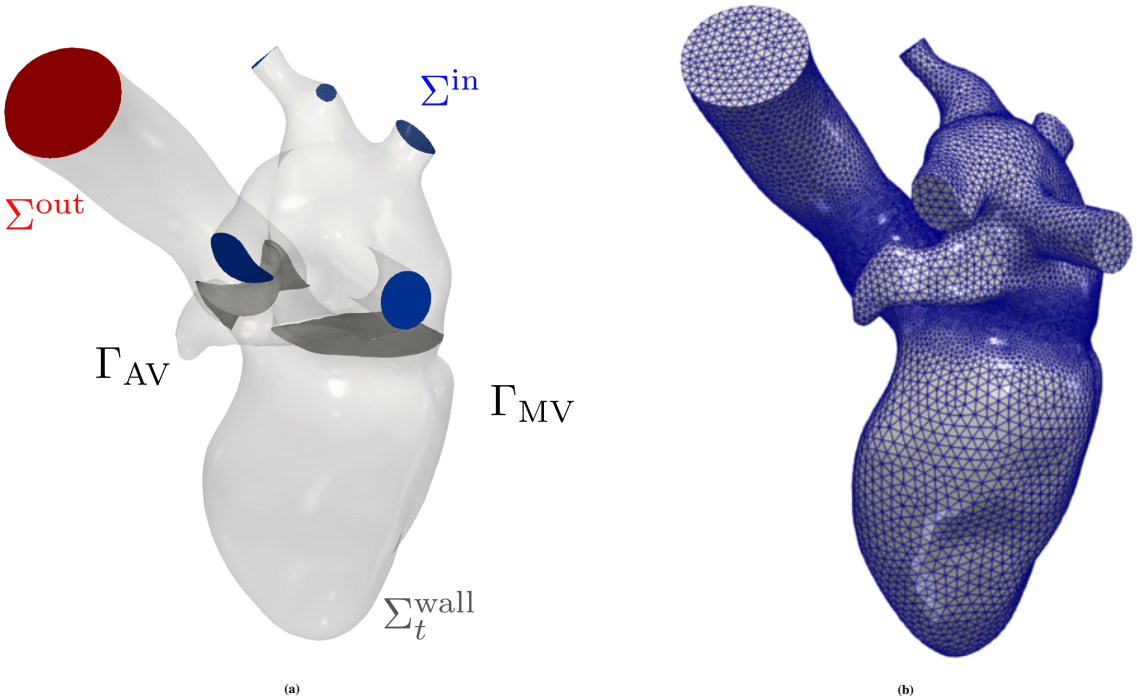

FIGURE 12 Test C. Left heart CFD domain highlighting boundary portions and immersed surfaces in their closed configurations (a); tetrahedral mesh generated for the CFD simulation (b).

k	R_k[kg/(m · s)]	ε_k[mm]	$\lvert\Gamma_k\rvert$[cm^2]	clos. time[s]	open. time[s]
MV	10^4	1.0	12.11	0.04725	0.49350
AV	10^4	1.0	5.41	0.38850	0.10600

TABLE 2 Test C. Parameters of the RIIS and ARIIS methods in the left heart CFD simulations.

h [mm]			cells [-]	DOFs ($\mathbb{P}_1 - \mathbb{P}_1$) [-]		
min	avg	max		**u**	p	total
0.44	1.44	6.40	645 699	333 243	111 081	444 324

TABLE 3 Test C. Mesh details for the left heart CFD simulations.

We set Neumann boundary conditions on the inlet and outlet sections of the domain by prescribing the pressure coming from the coupling between the 3D and the 0D circulation model, as explained in [14]. To prescribe the displacement field on the endocardium of the LV, we carry out an electromechanical simulation with the ventricular model proposed in [79]. We report the complete setup of the electromechanical model in Appendix A. Moreover, since the focus of the paper is the correct estimation of the ventricular pressure only, we neglect the motion of the remaining part of the domain by setting homogeneous Dirichlet boundary conditions on the wall of the left atrium and the ascending aorta. To avoid mesh element distortion, for the computation of K in Eq. (1), we use the boundary-based stiffening approach proposed in [81].

We generate the tethraedral mesh of the left heart displayed in Figure 12b with `vmtk` [82] using the methods and tools discussed in [83,25]. Mesh details are summarized in Table 3. We use as time-step size $\Delta t = 2.5 \times 10^{-4}$ s. Since the electromechanical simulation has a much larger timestep than the CFD one, we use smoothing splines [84] to approximate the electromechanical displacement field in time.

The values of R_k and ε_k of the RIIS method are provided in Table 2. These values of ε_k and R_k prevent flow through the closed immersed surfaces [56]. Moreover, following [56], we choose ε_k to guarantee that $\varepsilon_k \geq 1.5\, h_{min}$, where h_{min} is the minimum mesh

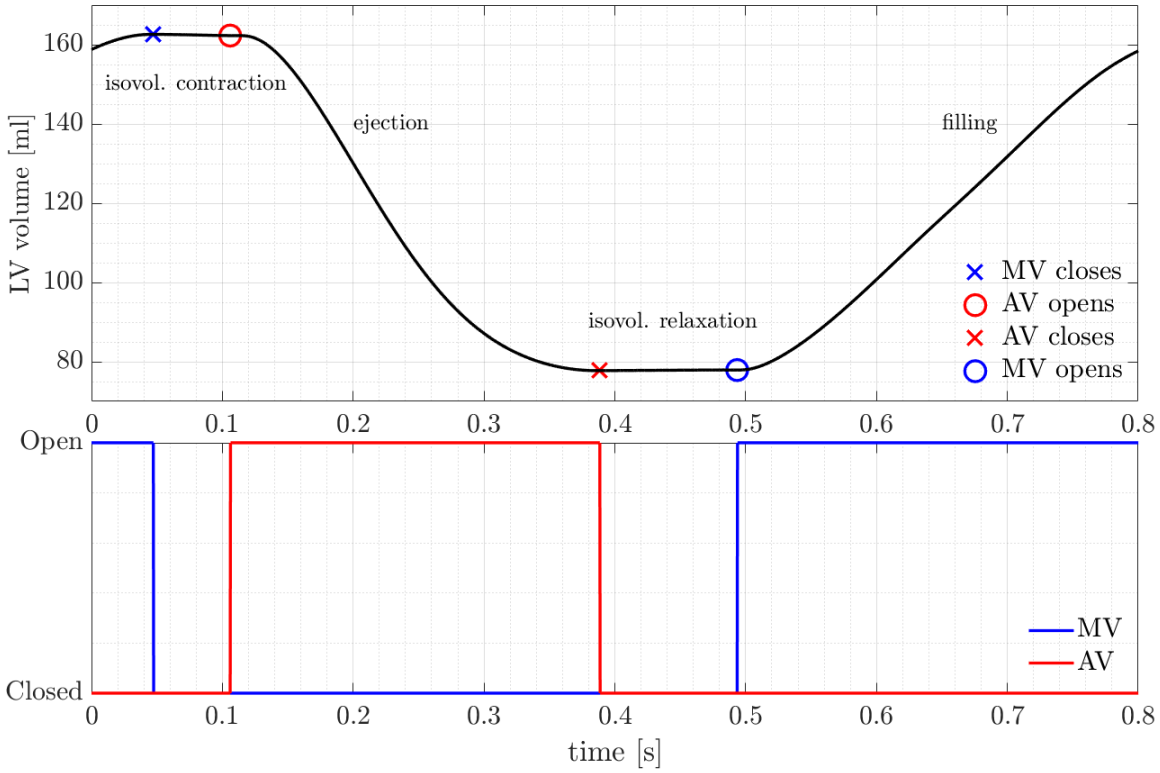

FIGURE 13 Test C. Volume of left ventricle, with opening and closing times for valves, and valve states.

size in the valves region. Since the condition number of the linear system associated to the FE discretization of (10) increases as the ratio R_k/ε_k increases, we choose the minimum value of R_k that guarantees impervious valves, as in[25]. In Table 2, we also report the areas of the valve sections needed for the ARIIS method. Moreover, as reference pressure $p^*(t)$, we use the one computed in the 3D-0D electromechanical ventricular model[79].

Numerical simulations are run in parallel using 48 cores from the GALILEO100 supercomputer at the CINECA supercomputing center.

3.3.1 | Comparison of RIIS and ARIIS methods

We carry out numerical simulations with the RIIS and the ARIIS methods. We simulate a single heartbeat of period $T = 0.8$ s. In Figure 13, we display the LV volume with the four heartbeat phases, along with the times corresponding to the begin and end of isovolumetric phases. We open and close the valves instantaneously (i.e. in one time step) at these times, also reported in Table 2. As reference pressure (p^*) for the ARIIS method, we use the LV pressure coming from the 3D cardiac electromechanical simulation coupled to the 0D cardiocirculatory model[79].

We display the ventricular pressure with the RIIS and ARIIS methods in Figure 14. We compute it by space-averaging the pressure in a control volume downwind of the MV. The RIIS method is not able to correctly capture the left ventricular pressure, yielding arbitrary pressure values during the isovolumetric phases, with unphysical oscillations. Differently, with the correction term introduced by the ARIIS method, the ventricular pressure follows the expected trend given by p^*. In addition, out of the isovolumetric phases, the pressure fields are almost identical between RIIS and ARIIS methods. Indeed, the correction term is active in the isovolumetric phases only, and it does not influence the remaining phases of the heart cycle, yielding a maximum discrepancy of 0.23 mmHg.

Furthermore, as shown in Figure 15, the largest discrepancies between p_{LV} and p^* in the ARIIS case is attained at the end of the isovolumetric phases. These discrepancies are related to the fact that the isovolumetric phases in realistic cardiac simulations are not exactly volume preserving. This happens due to, on the one hand, the projection of the displacement from the

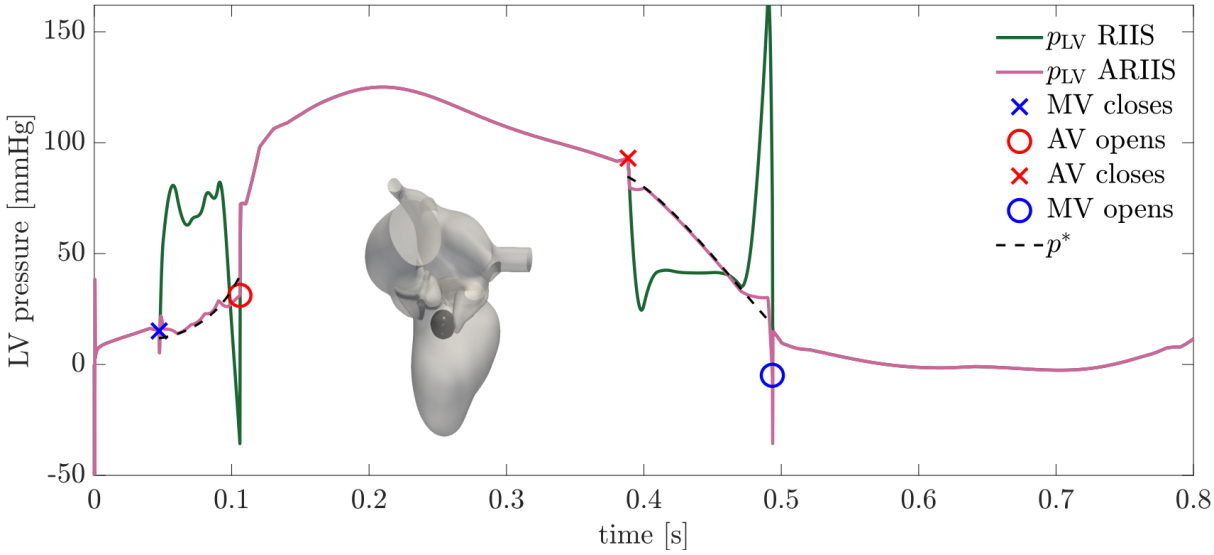

FIGURE 14 Test C. Ventricular and reference pressures for the left heart test case, with RIIS and ARIIS methods. p_{LV} is computed space-averaging the fluid pressure in the black control volume in the left ventricle.

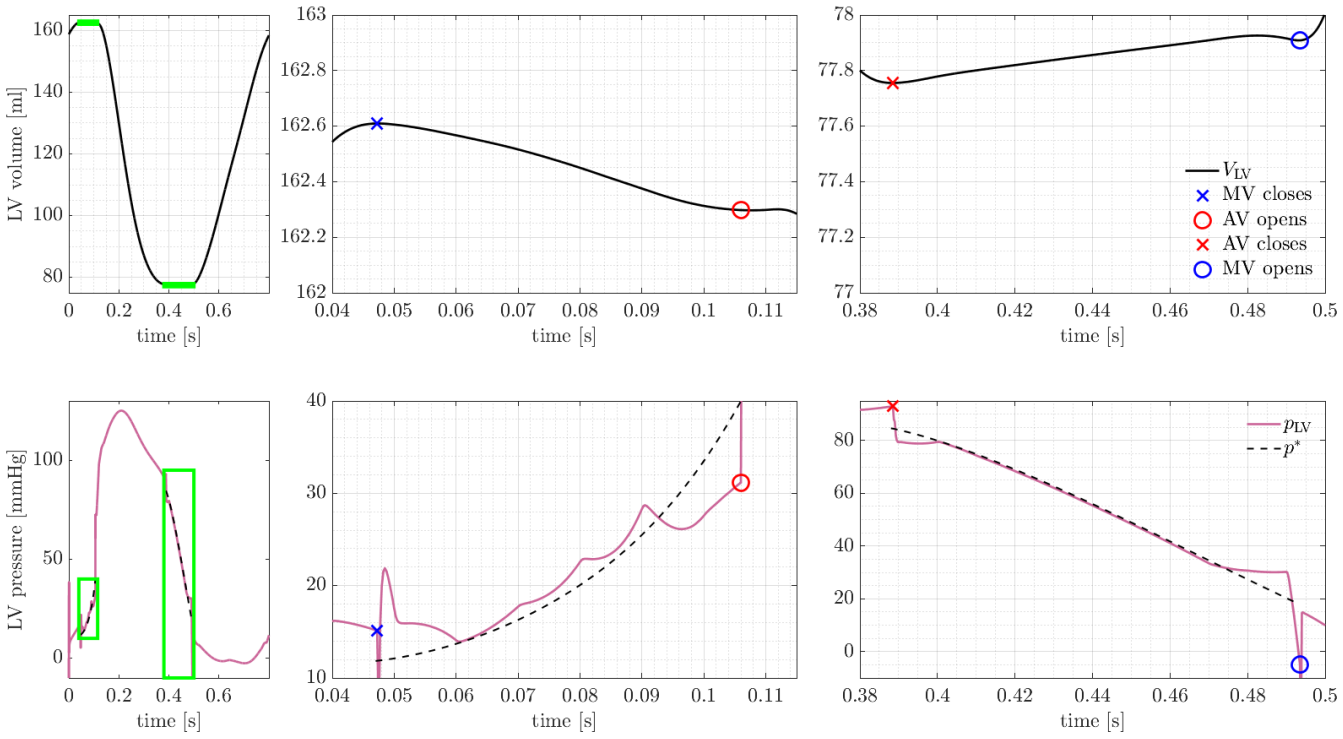

FIGURE 15 Test C. Ventricular volume and pressures (obtained through the ARIIS method), with zoom on the isovolumetric phases.

electromechanics (or imaging data) onto the fluid dynamics mesh and, on the other hand, the lifting problem in (1) that does not guarantee, a priori, any kind of volume conservation in the LV subdomain. Moreover, the displacement is characterized by small oscillations in time – introduced by the smoothing splines – that yield oscillations in the ventricular volume as well. Nonetheless, differently from the standard RIIS method, the proposed augmented approach allows to simulate the isovolumetric phases, with a pressure evolution that is much more similar to the heart physiology.

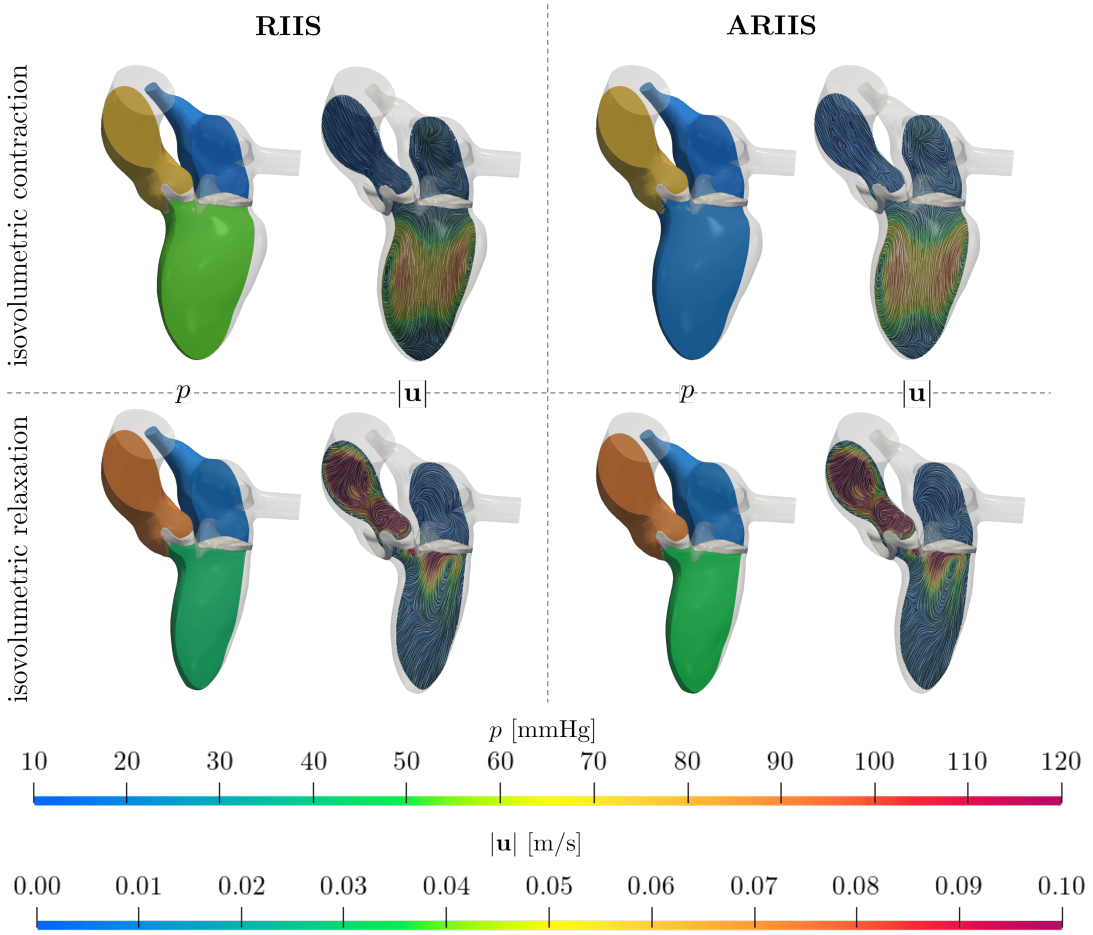

FIGURE 16 Test C. Comparison between RIIS and ARIIS methods during isovolumetric phases: pressure on a clip in the LV apico-basal direction and a section colored according to velocity magnitude with a surface LIC representation.

In Figure 16, we show the pressure field (in mmHg) on a clip in the LV apico-basal direction during the isovolumetric phases. The RIIS and ARIIS methods are characterized by different pressures, confirming our previous results. Moreover, we investigate the difference among the two solutions also in terms of velocity field, by showing a surface LIC representation on a slice in the LV apico-basal direction colored with velocity magnitude. Consistently with the findings of[24], we notice that the augmented approach does not impact the velocity field and both solutions reproduce the same flow patterns. More quantitatively, we compute the velocity magnitude in a control volume in the LV. When the augmented formulation is active, we compute a maximum discrepancy between the RIIS and the ARIIS velocities equal to 2.21×10^{-4} m/s, corresponding to a relative error (divided by the maximum RIIS velocity magnitude) equal to 0.29 %.

4 | CONCLUSIONS AND LIMITATIONS

In this paper, we proposed an augmented version of the Resistive Immersed Implicit Surface (RIIS) method[56] to correctly simulate the heart hemodynamics during isovolumetric phases. This Augmented RIIS (ARIIS) method extends the previously proposed Augmented Resistive Immersed Surface (ARIS) method[24] to the case of meshes that are non conforming to cardiac valves.

Starting from the RIIS method, we derived the correction term required to simulate the intracardiac hemodynamics when both valves are closed. Specifically, we introduced an additional term to the momentum balance of the Navier-Stokes equations that only acts on the valves and is only active during the isovolumetric phases. From the ARIIS derivation, we found that the corrective term depends on the external pressure, the valve areas, the resistive term itself, and a prescribed (reference) pressure

representing the intraventricular pressure transient when both valves are closed. The reference pressure can be imposed, for instance, from electromechanical simulations or from patient-specific data.

We applied the ARIIS method to three different problems: the same cylindrical toy problem introduced in[24] for the sake of validation of the proposed method, a novel benchmark problem retaining characteristics of a heart cycle, and the flow in a realistic human left heart geometry (with endocardium displacement obrtained from electromechanical simulations).

All tests showed that the ARIIS method yields a ventricular pressure that closely follows the prescribed reference evolution. Moreover, we found that the accuracy of the results is not affected by resistance coefficient values. On the other hand, we found that the error between measured and prescribed pressure decreases as the ratio ϵ/h_{min} increases, where ϵ is the half-thickness of the valve and h_{min} the minimum mesh size. This result is consistent with the RIIS method better capturing the immersed surface as the number of elements in the resistive surface thickness increases.

The ARIIS method is very sensitive to small volume variations and oscillations during isovolumetric phases. Thus, further investigations are advisable for the employment of a better interpolant or approximant (in time) of the input displacement field. Moreover, we observed some mismatch between the fluid pressure and the electromechanical one, yielding an unphysical jump from the isovolumetric contraction to the ejection phase. This mismatch suggests a deeper investigation of the similarities and differences between electromechanics and CFD models, which will be the subject of future work.

To conclude, the standard RIIS method yielded a ventricular pressure with large oscillations in time and inconsistent with physiology. On the contrary, the perturbation term introduced by the proposed ARIIS method provided a valid approach to produce a far more physiological ventricular pressure, and hence to correctly simulate the isovolumetric phases.

ACKNOWLEDGMENTS

AZ, LD and AQ received funding from the Italian Ministry of University and Research (MIUR) within the PRIN (Research projects of relevant national interest 2017 “Modeling the heart across the scales: from cardiac cells to the whole organ” Grant Registration number 2017AXL54F).

MB, IF, LD and AQ acknowledge the ERC Advanced Grant iHEART, “An Integrated Heart Model for the simulation of the cardiac function”, 2017–2022, P.I. A. Quarteroni (ERC–2016– ADG, project ID: 740132).

Finally, we gratefully acknowledge the CINECA award under the ISCRA initiative, for the availability of high performance computing resources and support under the projects IsC87_MCH, P.I. A. Zingaro, 2021-2022 and IsB25_MathBeat, P.I. A. Quarteroni, 2021-2022.

ETHICAL STATEMENT

None

Physics	Parameter		Value	
EP	Conductivities	$\sigma_{\mathrm{m}}^{\mathrm{l}}$	2.00×10^{-4}	m^2/s
		$\sigma_{\mathrm{m}}^{\mathrm{t}}$	1.05×10^{-4}	m^2/s
		$\sigma_{\mathrm{m}}^{\mathrm{n}}$	0.55×10^{-4}	m^2/s
	Stimulus	A_{app}	25.71	V/s
		σ_{app}	5×10^{-3}	m
		T_{app}	3×10^{-3}	s
AFG		γ	30	
		k_d	0.36	
		α_{k_d}	−0.2083	
		K_{off}	8	1/s
		K_{basic}	4	1/s
		μ_{fp}^0	32.255	1/s
		μ_{fp}^1	0.768	1/s
		a_{XB}	20×10^8	Pa
M	Guccione	c	8.8×10^2	Pa
		a_{ff}	8	
		a_{ss}	6	
		a_{nn}	3	
		a_{fs}	12	
		a_{fn}	3	
		a_{sn}	3	
		κ	5×10^4	Pa
	Boundary conditions	$K_{\perp}^{\mathrm{epi}}$	2×10^5	Pa/m
		$K_{\parallel}^{\mathrm{epi}}$	2×10^4	Pa/m
		$C_{\perp}^{\mathrm{epi}}$	2×10^4	$\mathrm{Pa} \cdot \mathrm{s/m}$
		$C_{\parallel}^{\mathrm{epi}}$	2×10^3	$\mathrm{Pa} \cdot \mathrm{s/m}$
	In. conditions	p_0	1333.2	Pa

TABLE A1 Parameters used in the electromechanical model: electrophysiology (EP), active force generation (AFG) and solid mechanics (M). For the force generation model, we only report parameters that are different from the original setting described in [85].

APPENDIX

A THE ELECTROMECHANICAL MODEL

We use the electromechanical model developed in [79]. In the following, we list the parameters employed to carry out the ventricular electromechanical simulation.

	Parameter	Value	
Systemic arteries	$R_{\text{AR}}^{\text{SYS}}$	0.3750	mmHg · s/mL
	$C_{\text{AR}}^{\text{SYS}}$	2.048	mL/mmHg
	$L_{\text{AR}}^{\text{SYS}}$	2.7×10^{-3}	mmHg · s^2/mL
	$R_{\text{upstream}}^{\text{SYS}}$	0.05	mmHg · s/mL
	$p_{\text{AR}}^{\text{SYS}}(0)$	80.0	Pa
	$Q_{\text{AR}}^{\text{SYS}}(0)$	0.0	mL/s
Systemic veins	$R_{\text{VEN}}^{\text{SYS}}$	0.26	mmHg · s/mL
	$C_{\text{VEN}}^{\text{SYS}}$	60.0	mL/mmHg
	$L_{\text{VEN}}^{\text{SYS}}$	5×10^{-4}	mmHg · s^2/mL
	$p_{\text{VEN}}^{\text{SYS}}(0)$	30.9	Pa
	$Q_{\text{VEN}}^{\text{SYS}}(0)$	0.0	mL/s
Pulmonary arteries	$R_{\text{AR}}^{\text{PUL}}$	0.05	mmHg · s/mL
	$C_{\text{AR}}^{\text{PUL}}$	10.0	mL/mmHg
	$L_{\text{AR}}^{\text{PUL}}$	5×10^{-4}	mmHg · s^2/mL
	$p_{\text{AR}}^{\text{PUL}}(0)$	29.34	Pa
	$Q_{\text{AR}}^{\text{PUL}}(0)$	0.0	mL/s
Pulmonary veins	$R_{\text{VEN}}^{\text{PUL}}$	0.025	mmHg · s/mL
	$C_{\text{VEN}}^{\text{PUL}}$	38.4	mL/mmHg
	$L_{\text{VEN}}^{\text{PUL}}$	2.083×10^{-4}	mmHg · s^2/mL
	$p_{\text{VEN}}^{\text{PUL}}(0)$	13.58	Pa
	$Q_{\text{VEN}}^{\text{PUL}}(0)$	0.0	mL/s

TABLE A2 Parameters of the circulation model for the ventricular electromechanical simulation: external circulation. The same parameters are employed for the 3D-0D CFD simulation.

	Parameter	Value	
Left atrium	E_A	0.07	mmHg/mL
	E_B	0.09	mmHg/mL
	t_C	0.80	
	T_C	0.17	
	T_R	0.17	
	$V_{LA}(0)$	79.5	mL
Right atrium	E_A	0.06	mmHg/mL
	E_B	0.07	mmHg/mL
	t_C	0.80	
	T_C	0.17	
	T_R	0.17	
	$V_{RA}(0)$	64.17	mL
Right ventricle	E_A	0.55	mmHg/mL
	E_B	0.05	mmHg/mL
	t_C	0.0	
	T_C	0.34	
	T_R	0.15	
	$V_{RV}(0)$	148.9	mL
Mitral valve	R_{min}	0.0164	mmHg · s/mL
	R_{max}	75 006.2	mmHg · s/mL
Aortic valve	R_{min}	0.0355	mmHg · s/mL
	R_{max}	75 006.2	mmHg · s/mL
Tricuspid valve	R_{min}	0.0075	mmHg · s/mL
	R_{max}	75 006.2	mmHg · s/mL
Pulmonary valve	R_{min}	0.0075	mmHg · s/mL
	R_{max}	75 006.2	mmHg · s/mL

TABLE A3 Parameters of the circulation model for the ventricular electromechanical simulation: cardiac circulation. Initial time of contraction t_c, contraction duration T_C and relaxation duration T_R are relative to the heartbeat period. For the right atrium, right ventricle, tricuspid and pulmonary valves, the same parameters are employed for the 3D-0D CFD simulation.

References

1. Formaggia L, Lamponi D, Tuveri M, Veneziani A. Numerical modeling of 1D arterial networks coupled with a lumped parameters description of the heart. *Computer methods in biomechanics and biomedical engineering* 2006; 9(5): 273–288.

2. Brenneisen J, Daub A, Gerach T, et al. Sequential coupling shows minor effects of fluid dynamics on myocardial deformation in a realistic whole-heart Model. *Frontiers in Cardiovascular Medicine* 2021; 8(December): 1–13. doi: 10.3389/fcvm.2021.768548

3. Bucelli M, Dede' L, Quarteroni A, Vergara C. Partitioned and monolithic FSI schemes for the numerical simulation of the heart. *Communications in Computational Physics (to appear)* 2022.

4. Cheng Y, Oertel H, Schenkel T. Fluid-structure coupled CFD simulation of the left ventricular flow during filling phase. *Annals of biomedical engineering* 2005; 33(5): 567–576.

5. Khodaei S, Henstock A, Sadeghi R, et al. Personalized intervention cardiology with transcatheter aortic valve replacement made possible with a non-invasive monitoring and diagnostic framework. *Scientific Reports* 2021; 11(1): 1–28.

6. Nordsletten D, McCormick M, Kilner P, Hunter P, Kay D, Smith N. Fluid–solid coupling for the investigation of diastolic and systolic human left ventricular function. *International Journal for Numerical Methods in Biomedical Engineering* 2011; 27(7): 1017–1039.

7. Zhang Q, Hisada T. Analysis of fluid–structure interaction problems with structural buckling and large domain changes by ALE finite element method. *Computer Methods in Applied Mechanics and Engineering* 2001; 190(48): 6341–6357.

8. Bucelli M, Zingaro A, Africa PC, Fumagalli I, Dede' L, Quarteroni AM. A mathematical model that integrates cardiac electrophysiology, mechanics and fluid dynamics: application to the human left heart. *arXiv preprint arXiv:2208.05551* 2022.

9. Santiago A, Aguado-Sierra J, Zavala-Aké M, et al. Fully coupled fluid-electro-mechanical model of the human heart for supercomputers. *International journal for numerical methods in biomedical engineering* 2018; 34(12): e3140.

10. Watanabe H, Hisada T, Sugiura S, Okada Ji, Fukunari H. Computer simulation of blood flow, left ventricular wall motion and their interrelationship by fluid-structure interaction finite element method. *JSME International Journal Series C Mechanical Systems, Machine Elements and Manufacturing* 2002; 45(4): 1003–1012.

11. Viola F, Meschini V, Verzicco R. Fluid–Structure-Electrophysiology interaction (FSE) in the left-heart: a multi-way coupled computational model. *European Journal of Mechanics-B/Fluids* 2020; 79: 212–232.

12. Choi YJ, Cfnstantino J, Vedula V, Trayanova N, Mittal R. A new MRI-based model of heart function with coupled hemodynamics and application to normal and diseased canine left ventricles. *Frontiers in bioengineering and biotechnology* 2015; 3: 140.

13. Tagliabue A, Dede L, Quarteroni A. Fluid dynamics of an idealized left ventricle: the extended Nitsche's method for the treatment of heart valves as mixed time varying boundary conditions. *International Journal for Numerical Methods in Fluids* 2017; 85(3): 135–164.

14. Zingaro A, Dede' L, Menghini F, Quarteroni A. Hemodynamics of the heart's left atrium based on a Variational Multiscale-LES numerical method. *European Journal of Mechanics-B/Fluids* 2021; 89: 380–400.

15. Domenichini F, Pedrizzetti G, Baccani B. Three-dimensional filling flow into a model left ventricle. *Journal of fluid mechanics* 2005; 539: 179–198.

16. Baccani B, Domenichini F, Pedrizzetti G. Vortex dynamics in a model left ventricle during filling. *European Journal of Mechanics-B/Fluids* 2002; 21(5): 527–543.

17. Mittal R, Seo JH, Vedula V, et al. Computational modeling of cardiac hemodynamics: current status and future outlook. *Journal of Computational Physics* 2016; 305: 1065–1082.

18. Corti M, Zingaro A, Dede' L, Quarteroni A. Impact of Atrial Fibrillation on Left Atrium Haemodynamics: A Computational Fluid Dynamics Study. *arXiv preprint arXiv:2202.10893* 2022.

19. Fumagalli I, Fedele M, Vergara C, et al. An image-based computational hemodynamics study of the Systolic Anterior Motion of the mitral valve. *Computers in Biology and Medicine* 2020; 123: 103922.

20. This A, Morales HG, Bonnefous O, Fernández MA, Gerbeau JF. A pipeline for image based intracardiac CFD modeling and application to the evaluation of the PISA method. *Computer Methods in Applied Mechanics and Engineering* 2020; 358: 112627.

21. Chnafa C, Mendez S, Nicoud F. Image-based large-eddy simulation in a realistic left heart. *Computers & Fluids* 2014; 94: 173–187.

22. Masci A, Alessandrini M, Forti D, et al. A proof of concept for computational fluid dynamic analysis of the left atrium in atrial fibrillation on a patient-specific basis. *Journal of Biomechanical Engineering* 2020; 142(1).

23. Augustin CM, Crozier A, Neic A, et al. Patient-specific modeling of left ventricular electromechanics as a driver for haemodynamic analysis. *EP Europace* 2016; 18(suppl_4): iv121–iv129.

24. This A, Boilevin-Kayl L, Fernández MA, Gerbeau JF. Augmented Resistive Immersed Surfaces valve model for the simulation of cardiac hemodynamics with isovolumetric phases. *International journal for numerical methods in biomedical engineering* 2020; 36(3): e3223.

25. Zingaro A, Fumagalli I, Dede' L, et al. A geometric multiscale model for the numerical simulation of blood flow in the human left heart. *Discrete and Continous Dynamical System - S* 2022; 15(8): 2391-2427.

26. Cheng R, Lai YG, Chandran KB. Three-dimensional fluid-structure interaction simulation of bileaflet mechanical heart valve flow dynamics. *Annals of Biomedical Engineering* 2004; 32(11): 1471–1483.

27. Espino DM, Shepherd DE, Hukins DW. Evaluation of a transient, simultaneous, arbitrary Lagrange–Euler based multi-physics method for simulating the mitral heart valve. *Computer Methods in Biomechanics and Biomedical Engineering* 2014; 17(4): 450–458. doi: 10.1080/10255842.2012.688818

28. Basting S, Quaini A, Čanić S, Glowinski R. Extended ALE method for fluid–structure interaction problems with large structural displacements. *Journal of Computational Physics* 2017; 331: 312–336. doi: 10.1016/j.jcp.2016.11.043

29. Jianhai Z, Dapeng C, Shengquan Z. ALE finite element analysis of the opening and closing process of the artificial mechanical valve. *Applied Mathematics and Mechanics* 1996; 17(5): 403–412. doi: 10.1007/BF00131088

30. Nestola MGC, Faggiano E, Vergara C, et al. Computational comparison of aortic root stresses in presence of stentless and stented aortic valve bio-prostheses. *Computer methods in biomechanics and biomedical engineering* 2017; 20(2): 171–181. doi: 10.1080/10255842.2016.1207171

31. Fernández MA, Gerbeau JF, Martin V. Numerical simulation of blood flows through a porous interface. *ESAIM: Mathematical Modelling and Numerical Analysis* 2008; 42(6): 961–990.

32. Astorino M, Hamers J, Shadden SC, Gerbeau JF. A robust and efficient valve model based on resistive immersed surfaces. *International Journal for Numerical Methods in Biomedical Engineering* 2012; 28(9): 937–959.

33. Alauzet F, Fabrèges B, Fernández MA, Landajuela M. Nitsche-XFEM for the coupling of an incompressible fluid with immersed thin-walled structures. *Computer Methods in Applied Mechanics and Engineering* 2016; 301: 300–335.

34. Hansbo P, Larson MG, Zahedi S. Characteristic cut finite element methods for convection–diffusion problems on time dependent surfaces. *Computer Methods in Applied Mechanics and Engineering* 2015; 293: 431–461.

35. Burman E, Fernández MA. An unfitted Nitsche method for incompressible fluid–structure interaction using overlapping meshes. *Computer Methods in Applied Mechanics and Engineering* 2014; 279: 497–514.

36. Mayer UM, Popp A, Gerstenberger A, Wall WA. 3D fluid–structure–contact interaction based on a combined XFEM FSI and dual mortar contact approach. *Computational Mechanics* 2010; 46(1): 53–67.

37. Massing A, Larson M, Logg A, Rognes M. A Nitsche-based cut finite element method for a fluid-structure interaction problem. *Communications in Applied Mathematics and Computational Science* 2015; 10(2): 97–120.

38. Gerstenberger A, Wall WA. An extended finite element method/Lagrange multiplier based approach for fluid–structure interaction. *Computer Methods in Applied Mechanics and Engineering* 2008; 197(19-20): 1699–1714.

39. Zonca S, Vergara C, Formaggia L. An unfitted formulation for the interaction of an incompressible fluid with a thick structure via an XFEM/DG approach. *SIAM Journal on Scientific Computing* 2018; 40(1): B59–B84.

40. Spühler JH, Jansson J, Jansson N, Hoffman J. 3D fluid-structure interaction simulation of aortic valves using a unified continuum ALE FEM model. *Frontiers in physiology* 2018; 9: 363.

41. Peskin CS. Flow patterns around heart valves: A numerical method. *Journal of Computational Physics* 1972; 10(2): 252 - 271. doi: 10.1016/0021-9991(72)90065-4

42. Borazjani I, Ge L, Sotiropoulos F. High-resolution fluid–structure interaction simulations of flow through a bi-leaflet mechanical heart valve in an anatomic aorta. *Annals of Biomedical Engineering* 2010; 38(2): 326–344. doi: 10.1007/s10439-009-9807-x

43. Griffith BE. Immersed boundary model of aortic heart valve dynamics with physiological driving and loading conditions. *International Journal for Numerical Methods in Biomedical Engineering* 2012; 28(3): 317–345. doi: 10.1002/cnm.1445

44. Hsu MC, Kamensky D, Bazilevs Y, Sacks MS, Hughes TJR. Fluid–structure interaction analysis of bioprosthetic heart valves: significance of arterial wall deformation. *Computational Mechanics* 2014; 54(4): 1055–1071. doi: 10.1007/s00466-014-1059-4

45. Wu MC, Zakerzadeh R, Kamensky D, Kiendl J, Sacks MS, Hsu MC. An anisotropic constitutive model for immersogeometric fluid–structure interaction analysis of bioprosthetic heart valves. *Journal of biomechanics* 2018; 74: 23–31. doi: 10.1016/j.jbiomech.2018.04.012

46. Liu WK, Liu Y, Farrell D, et al. Immersed finite element method and its applications to biological systems. *Computer methods in applied mechanics and engineering* 2006; 195(13-16): 1722–1749. doi: 10.1016/j.cma.2005.05.049

47. Yang J, Yu F, Krane M, Zhang LT. The Perfectly Matched Layer absorbing boundary for fluid–structure interactions using the Immersed Finite Element Method. *Journal of fluids and structures* 2018; 76: 135–152. doi: 10.1016/j.jfluidstructs.2017.09.002

48. Nestola MGC, Becsek B, Zolfaghari H, et al. An immersed boundary method for fluid-structure interaction based on variational transfer. *Journal of computational physics* 2019; 398: 108884. doi: 10.1016/j.jcp.2019.108884

49. Glowinski R, Pan TW, Periaux J. A Lagrange multiplier/fictitious domain method for the numerical simulation of incompressible viscous flow around moving rigid bodies:(I) case where the rigid body motions are known a priori. *Comptes Rendus de l'Académie des Sciences-Series I-Mathematics* 1997; 324(3): 361–369. doi: 10.1016/S0764-4442(99)80376-0

50. Astorino M, Gerbeau JF, Pantz O, Traore KF. Fluid–structure interaction and multi-body contact: application to aortic valves. *Computer Methods in Applied Mechanics and Engineering* 2009; 198(45-46): 3603–3612. doi: 10.1016/j.cma.2008.09.012

51. Bazilevs Y, Hsu MC, Kiendl J, Wüchner R, Bletzinger KU. 3D simulation of wind turbine rotors at full scale. Part II: Fluid–structure interaction modeling with composite blades. *International Journal for Numerical Methods in Fluids* 2011; 65(1-3): 236–253. doi: 10.1002/fld.2454

52. Kamensky D, Hsu MC, Schillinger D, et al. An immersogeometric variational framework for fluid–structure interaction: Application to bioprosthetic heart valves. *Computer methods in applied mechanics and engineering* 2015; 284: 1005–1053. doi: 10.1016/j.cma.2014.10.040

53. De Hart J, Peters G, Schreurs P, Baaijens F. A three-dimensional computational analysis of fluid–structure interaction in the aortic valve. *Journal of biomechanics* 2003; 36(1): 103–112. doi: 10.1016/s0021-9290(02)00244-0

54. Loon vR, Anderson PD, Vosse v. dFN. A fluid–structure interaction method with solid-rigid contact for heart valve dynamics. *Journal of Computational Physics* 2006; 217(2): 806–823. doi: 10.1016/j.jcp.2006.01.032

55. Morsi YS, Yang WW, Wong CS, Das S. Transient fluid–structure coupling for simulation of a trileaflet heart valve using weak coupling. *Journal of Artificial Organs* 2007; 10(2): 96–103. doi: 10.1007/s10047-006-0365-9

56. Fedele M, Faggiano E, Dede' L, Quarteroni A. A patient-specific aortic valve model based on moving resistive immersed implicit surfaces. *Biomechanics and Modeling in Mechanobiology* 2017; 16(5): 1779–1803. doi: 10.1007/s10237-017-0919-1

57. Marom G. Numerical methods for fluid–structure interaction models of aortic valves. *Archives of Computational Methods in Engineering* 2015; 22(4): 595–620. doi: 10.1007/s11831-014-9133-9

58. Votta E, Le TB, Stevanella M, et al. Toward patient-specific simulations of cardiac valves: state-of-the-art and future directions. *Journal of Biomechanics* 2013; 46(2): 217–228. doi: 10.1016/j.jbiomech.2012.10.026

59. Hirschhorn M, Tchantchaleishvili V, Stevens R, Rossano J, Throckmorton A. Fluid–structure interaction modeling in cardiovascular medicine–A systematic review 2017–2019. *Medical engineering & physics* 2020; 78: 1–13.

60. Schenkel T, Malve M, Reik M, Markl M, Jung B, Oertel H. MRI-based CFD analysis of flow in a human left ventricle: methodology and application to a healthy heart. *Annals of biomedical engineering* 2009; 37(3): 503–515.

61. Bavo A, Pouch AM, Degroote J, et al. Patient-specific CFD models for intraventricular flow analysis from 3D ultrasound imaging: Comparison of three clinical cases. *Journal of biomechanics* 2017; 50: 144–150.

62. Quarteroni A, Sacco R, Saleri F. *Numerical mathematics*. 37. Springer Science & Business Media . 2010.

63. Doyle MG, Tavoularis S, Bougault Y. Application of fluid-structure interaction to numerical simulations in the left ventricle. *Transactions of the Canadian Society for Mechanical Engineering* 2015; 39(4): 749–766.

64. Perktold K, Thurner E, Kenner T. Flow and stress characteristics in rigid walled and compliant carotid artery bifurcation models. *Medical & biological engineering & computing* 1994; 32(1): 19–26.

65. Taylor CA, Hughes TJ, Zarins CK. Finite element modeling of blood flow in arteries. *Computer methods in applied mechanics and engineering* 1998; 158(1-2): 155–196.

66. Formaggia L, Quarteroni A, Veneziani A. *Cardiovascular Mathematics: Modeling and simulation of the circulatory system*. 1. Springer Science & Business Media . 2010.

67. Quarteroni A, Dede' L, Manzoni A, Vergara C, others . *Mathematical modelling of the human cardiovascular system: data, numerical approximation, clinical applications*. 33. Cambridge University Press . 2019.

68. Donea J, Giuliani S, Halleux JP. An arbitrary Lagrangian-Eulerian finite element method for transient dynamic fluid-structure interactions. *Computer Methods in Applied Mechanics and Engineering* 1982; 33(1-3): 689–723.

69. Hughes TJ, Liu WK, Zimmermann TK. Lagrangian-Eulerian finite element formulation for incompressible viscous flows. *Computer Methods in Applied Mechanics and Engineering* 1981; 29(3): 329–349.

70. Tezduyar T. Stabilized Finite Element Formulations for Incompressible Flow Computations. In: Hutchinson JW, Wu TY., eds. *Advances in Applied Mechanics*. 28. Elsevier. 1991 (pp. 1-44)

71. Bazilevs Y, Calo V, Cottrell J, Hughes TJR, Reali A, Scovazzi G. Variational multiscale residual-based turbulence modeling for large eddy simulation of incompressible flows. *Computer Methods in Applied Mechanics and Engineering* 2007; 197(1-4): 173–201. doi: 10.1016/j.cma.2007.07.016

72. Forti D, Dede' L. Semi-implicit BDF time discretization of the Navier–Stokes equations with VMS-LES modeling in a High Performance Computing framework. *Computers & Fluids* 2015; 117: 168–182. doi: 10.1016/j.compfluid.2015.05.011

73. Africa PC. life^x: a flexible, high performance library for the numerical solution of complex finite elements. *arXiv:2207.14668* 2022.

74. Arndt D, Bangerth W, Blais B, et al. The deal.II library, Version 9.3. *J. Numer. Math.* 2021; 29.

75. Arndt D, Bangerth W, Davydov D, et al. The `deal.II` finite element library: design, features, and insights. *Computers & Mathematics with Applications* 2020. doi: 10.1016/j.camwa.2020.02.022

76. Official `deal.ii` website. https://www.dealii.org/; .

77. Blanco PJ, Feijoo RA. A 3D-1D-0D Computational Model for the Entire Cardiovascular System. *Mecanica Computacional* 2010; 24: 5887–5911.

78. Hirschvogel M, Bassilious M, Jagschies L, Wildhirt SM, Gee MW. A monolithic 3D-0D coupled closed-loop model of the heart and the vascular system: Experiment-based parameter estimation for patient-specific cardiac mechanics. *International Journal for Numerical Methods in Biomedical Engineering* 2017; 33(8): e2842. doi: 10.1002/cnm.2842

79. Regazzoni F, Salvador M, Africa P, Fedele M, Dedè L, Quarteroni A. A cardiac electromechanical model coupled with a lumped-parameter model for closed-loop blood circulation. *Journal of Computational Physics* 2022; 457: 111083. doi: https://doi.org/10.1016/j.jcp.2022.111083

80. Inc ZMG. Zygote Solid 3D Heart Generation II Development Report. *Technical Development of 3D Anatomical Systems* 2014.

81. Jasak H, Tukovic Z. Automatic mesh motion for the unstructured finite volume method. *Transactions of FAMENA* 2006; 30(2): 1–20.

82. Antiga L, Piccinelli M, Botti L, Ene-Iordache B, Remuzzi A, Steinman DA. An image-based modeling framework for patient-specific computational hemodynamics. *Medical & Biological Engineering & Computing* 2008; 46(11): 1097–1112. doi: 10.1007/s11517-008-0420-1

83. Fedele M, Quarteroni AM. Polygonal surface processing and mesh generation tools for numerical simulations of the complete cardiac function. *Int. J. Numer. Meth. Bio.* 2021; 37: e3435.

84. De Boor C. *A practical guide to splines*. 27. springer-verlag New York . 1978.

85. Regazzoni F, Dedè L, Quarteroni A. Biophysically detailed mathematical models of multiscale cardiac active mechanics. *PLoS computational biology* 2020; 16(10): e1008294.

MOX Technical Reports, last issues

Dipartimento di Matematica
Politecnico di Milano, Via Bonardi 9 - 20133 Milano (Italy)

57/2022 Ruffino, L.; Santoro, A.; Sparvieri, S.; Regazzoni, F.; Adebo, D.A.; Quarteroni, A.; Vergara, C
Computational analysis of cardiovascular effects of COVID- 19 infection in children

56/2022 Africa, P.C.
lifex: a flexible, high performance library for the numerical solution of complex finite element problems

54/2022 Bucelli, M.; Zingaro, A.; Africa, P. C.; Fumagalli, I.; Dede', L.; Quarteroni, A.
A mathematical model that integrates cardiac electrophysiology, mechanics and fluid dynamics: application to the human left heart

55/2022 Cavinato, L.; Pegoraro, M.; Ragni, A.; Ieva, F.
Imaging-based representation and stratification of intra-tumor Heterogeneity via tree-edit distance

52/2022 Fedele, M.; Piersanti, R.; Regazzoni, F.; Salvador, M.; Africa, P. C.; Bucelli, M.; Zingaro, A.; I
A comprehensive and biophysically detailed computational model of the whole human heart electromechanics

51/2022 Losapio, D.; Scotti, A.
Local Embedded Discrete Fracture Model (LEDFM)

53/2022 Antonietti, P.F; Cauzzi, C.; Mazzieri, I.; Melas L.; Stupazzini, M.
Numerical simulation of the Athens 1999 earthquake including simplified models of the Acropolis and the Parthenon: initial results and outlook

50/2022 Elías, A.; Jiménez, R.; Paganoni, A.M.; Sangalli, L.M.
Integrated Depths for Partially Observed Functional Data

47/2022 Botti, M.; Di Pietro, D.A.; Salah, M.
A serendipity fully discrete div-div complex on polygonal meshes

48/2022 Gregorio, C.; Barbati, G.; Ieva, F.
A wavelet-mixed landmark survival model for the effect of short-term oscillations in longitudinal biomarker's profiles